



저작자표시-비영리-변경금지 2.0 대한민국

이용자는 아래의 조건을 따르는 경우에 한하여 자유롭게

- 이 저작물을 복제, 배포, 전송, 전시, 공연 및 방송할 수 있습니다.

다음과 같은 조건을 따라야 합니다:



저작자표시. 귀하는 원저작자를 표시하여야 합니다.



비영리. 귀하는 이 저작물을 영리 목적으로 이용할 수 없습니다.



변경금지. 귀하는 이 저작물을 개작, 변형 또는 가공할 수 없습니다.

- 귀하는, 이 저작물의 재이용이나 배포의 경우, 이 저작물에 적용된 이용허락조건을 명확하게 나타내어야 합니다.
- 저작권자로부터 별도의 허가를 받으면 이러한 조건들은 적용되지 않습니다.

저작권법에 따른 이용자의 권리는 위의 내용에 의하여 영향을 받지 않습니다.

이것은 [이용허락규약\(Legal Code\)](#)을 이해하기 쉽게 요약한 것입니다.

[Disclaimer](#)

공학박사 학위논문

**Effect of Nanoscopic Confinement on
Self-Assembled Nanostructures of
Block Copolymers**

나노간힘효과가 블록공중합체의
자기조립 나노구조에 미치는 영향

2019년 8월

서울대학교 대학원

화학생물공학부

김 영 결

Abstract

Effect of Nanoscopic Confinement on Self-Assembled Nanostructures of Block Copolymers

Youngkeol Kim

School of Chemical and Biological Engineering

The Graduate School

Seoul National University

Block copolymers (BCPs) consisting of two distinctive polymer chains can self-organize into ordered nanoscale structures. Their self-assembled morphologies depend primarily on the volume ratio of the constituent blocks, chain length, and interaction between the segments. To further develop and control their nanostructures and optimize corresponding properties, a variety of methods such as solvent annealing, additives, surface treatment, and confinement have been introduced. The self-assembled structures of BCP under nanoscale confinement

exhibit distinctive nanostructures, which do not appear in the bulk state. Particularly, the ordering process of block copolymers and the resulting morphologies are significantly determined by the dimensionality, geometry, and surface property of the confining environment. Development of controllable nanostructures under confinement has received much attention due to the possibility to achieve novel structures with potential applications such as lithography, photonic crystals, plasmonics, filtration, photovoltaic devices, and so on.

Various types of confinement using thin films, porous membranes, and emulsion droplets have been investigated both experimentally and computationally. It has been demonstrated that under confined states, besides the intrinsic properties of polymers, external factors including size, shape, surface properties, and dimensionality of the external confining environment were also crucial to the phase-separated morphologies. In this study, systematic studies of nanoconfinement effect on the structural properties of diblock copolymers will be discussed. We applied nanoconfinement effect using porous anodized aluminum oxide templates and the shape and size of confining environment is controlled to investigate the underlying principle of the phase-behavior of BCPs under confinement. Also, to diversify the BCP nanostructures, new approaches such as the addition of homopolymer or surface modification was performed.

In the first Chapter, fundamentals on block copolymers, directed self-assembly (DSA) and nanoconfinement effects upon the dimension of outer environment will be described to address the importance and effectiveness of our approach.

In the second Chapter, we present the fabrication of anodic aluminum oxide template with nanopore of various geometries which can be used for not only confining environment, but template-assisted synthesis. The physical size of the

nanomaterials such as diameter of nanoparticles or thickness or thin films as well as their shape is controllable at nanoscopic scale, which have enabled quantitative as well as qualitative analysis of the materials and made the materials exploited as building blocks for an advanced material with desirable properties. Furthermore, Anisotropic geometries can break the symmetry of molecular packing under confinement and the frustration of assembled molecules are maximized in a singularity point which leads to unconventional assembly of chained molecules and novel nanostructures which is not observed. With engineering the synthetic method, anisotropy in two different plane was demonstrated. Specifically, trigonal pores have anisotropy in XY-plane and conical pores in z-axis. It is demonstrated that physical properties including shape and size could be controlled for desired purpose. Also, to facilitate nanostructured template easily, we developed nano-imprinting technique to make positive and negative mold replicating the AAO templates.

In Chapter 3, we studied the phase transition behavior of block copolymers using two different methods: addition of homopolymer and surface treatment using organosilicate. Firstly, Block copolymer/homopolymer binary blends in cylindrical confinement was investigated in comparison with that in the bulk state. The phase behavior of lamellae-forming poly(styrene-*b*-1,4-butadiene) (PS-*b*-PB) in both bulk and 2D confinement were examined with different chain length and weight fraction of homopolymers. By the comparative study of bulk and confined states, we conclude that the effect of hPS addition on the phase transition of BCP was significantly enhanced in the nanoscale 2D confinement compared to the bulk state. Constraints caused by confinement make the phase transition of BCPs more sensitive to the addition of homopolymers, and at the same time the homopolymer chains relieve the stress which copolymer chains experience under confinement. Secondly,

we changed the surface properties of AAO templates via organosilicate (OS) interlayer coating. Under 2D confinement, the phase-separation of BCPs significantly depends upon the degree of confinement and interaction between the environment. However, most previous studies have only focused on the effects of confinement on the self-assembly of BCP. Here, we used organosilicate (OS) which the surface energy could be easily controlled by thermal process as an interlayer to identify the morphologies of BCPs as a function of interfacial energies. The OS interlayer was coated on inner surface of anodized aluminum oxide (AAO) pores by template-wetting method and cured in a range of temperature to control the surface energy of interlayer. Lamellae-forming poly(styrene-*b*-methyl methacrylate) (PS-*b*-PMMA) (SMA) was injected in the OS-coated AAO pores in the melt by capillary forces. With detailed analysis, we could identify that the self-assembly of SMA in 2D confinement is competitively affected by entropic and enthalpic effects as interfacial energy is changed. As simply controlling the curing temperature of OS interlayer, various morphologies arising from both the preferential wetting behavior and neutral wetting behavior were identified. This work provides the proof-of-principle of microdomain transitions in self-assembled BCP under cylindrically confined geometry.

In Chapter 4, we report a strategy to control the morphologies of poly(styrene-*b*-1,4 butadiene) (PS-*b*-PB) confined within conical nanopores. While previous work studied the self-assembly of chained molecules under confinement using symmetric environment such as cylinders and spheres, the phase-behavior of block copolymers within asymmetric geometries has rarely been addressed so far. With both experimental and theoretical analyses of the geometric effects of conical nanopores, we systematically investigate the competitive interplay of thermodynamic

parameters on the self-assembly of block copolymers within asymmetric geometry. The size, shape, and surface properties of the nanopores were controlled in order to investigate enthalpic and entropic factors on the self-assembly of BCPs. The loss of conformational entropy induced by the large curvature at the vertices was the critical parameter to determine the orientation of BCP microdomains within such asymmetric pores. Specifically, while stacked lamellae perpendicular to the depth were observed for small-sized conical pores, concentric lamellae replicating the geometry of confining matrix were obtained in large cones and cylindrical pores. As the size and shape of the pores were varied, intermediate morphologies were also obtained. Computational results based on the simulated annealing method with parameters matched to experiment was also calculated to compare observed morphologies. Calculated results relating to the interfacial energies between blocks, the entropic penalty induced by chain stretching, and the surface energy between blocks and pore wall were quantitatively described in order to elucidate how the interplay between thermodynamic factors contributed to the equilibrium morphologies. 3D imaging of transmission electron microtomography was also performed in an attempt to gain more detailed information on the internal nanostructures of BCP.

Keyword: Block Copolymers, Nano-Confinement, Directed Self-Assembly, Anodic Aluminum Oxide Templates, Nanostructures

Student Number : 2014-21522

Contents

Chapter 1. Introduction	1
1.1. Fundamentals on Block Copolymers	1
1.1.1. Introduction to Block Copolymers.....	1
1.1.2. Directed Self-Assembly of Block Copolymers.....	4
1.2. Phase-Behavior of Block Copolymers under Nanoconfinement	6
1.2.1. Self-Assembly of Block Copolymers under 1D Nanoconfinement ...	6
1.2.2. Self-Assembly of Block Copolymers under 2D Nanoconfinement ...	9
1.2.3. Self-Assembly of Block Copolymers under 3D Nanoconfinement .	11
Chapter 2. Development of Anodic Aluminum Oxide Template with Nanopores of Various Geometries for Confining Environment	13
2.1. Introduction.....	13
2.2. Effect of Asymmetric Geometry on Confined Self-Assembly.....	17
2.2.1. AAO Templates with Cylindrical Nanopores.....	17
2.2.2. Effect of Asymmetric Geometry on the Self-Assembly of Block Copolymers	21
2.3. Development AAO Templates with Conical Nanopores.....	24
2.3.1. Experimental	24
2.3.2. Results and Discussion	27
2.4. Development AAO Templates with Trigonal Nanopores.....	33
2.3.1. Experimental.....	33
2.3.2. Results and Discussion	36
2.5. Pattern Transfer of Ordered Nanostructures	40
2.5.1. Experimental.....	40
2.5.2. Results and Discussion	41
2.6. Conclusion	44

Chapter 3. Morphological Transition of Block Copolymer within Cylindrical Channels 45

3.1. Introduction.....	45
3.2. Experimental.....	50
3.2.1. Block Copolymer/Homopolymer AB/A Binary Blends within Cylindrical Channels.....	50
3.2.2. Tunable Surface Energy Interlayer Coating to Control the Phase Behavior of Block Copolymers in 2D Confinement.....	54
3.2.3. Characterization.....	55
3.3. Results and Discussion.....	56
3.3.1. Microdomain Transition of Binary Blends with Low Molecular Weight hPS in 2D Confinement.....	56
3.3.2. Comparison of the Effect of hPS Weight Fraction on the Phase Transitions in the Bulk and Confined States.....	59
3.3.3. Effect of Mn,hPS/Mn,PS Block on the Phase Transitions in Bulk and Confined States.....	61
3.3.4. Tunable Surface Energy of OS Coating to Control the Orientation of Block Copolymers.....	68
3.3.5. OS Interlayer Coating on AAO templates to Control the Orientation of Block Copolymers within Cylindrical Nano-Channels.....	74
3.4. Conclusion.....	78

Chapter 4. Self-Assembled Morphologies of Block Copolymers Confined in Conical Nanopores 79

4.1. Introduction.....	79
4.2. Experimental.....	82
4.3. Results and Discussion.....	87
4.3.1. Self-Assembled Morphologies of Block Copolymer within Conical Nanopores.....	87
4.3.2. Effect of Bottom Geometry on Chain Conformation of Block Copolymers.....	94
4.3.3. Changes in Wetting Behavior of Block Copolymer Confined within	

Conical Nanopores.....	98
4.3.4. Effect of Molecular Weight of Block Copolymers	101
4.3.5. Enthalpic and Entropic Contribution in the Free Energy of Block Copolymers within Conical Confinement.....	103
4.4. Conclusion	107
 Bibliography.....	 108
국문초록	119

List of Tables

Table 2.1. Pore dimension including interpore distance (D_{int}) and pore diameter (D_P) depending on the type of electrolytes and output voltage for anodization.....	19
Table 3.1. Detailed information of PS- <i>b</i> -PBD/hPS binary blends.....	52
Table 3.2. Contact angles of water and diiodomethane on OS substrates and surface energy divided by dispersive and polar fraction of OS cured at different temperature	69
Table 4.1. List of various types of pore and their diameter (D_P), radius of curvature at the bottom (r_c), and aspect ratio ($AR = h/D_P$).....	84

List of Figures

Figure 1.1. Schematic illustration of phase behavior and nanostructures of diblock copolymer depending on the volume fraction of each block2

Figure 1.2. Schematic illustration of the phase behavior of diblock copolymer under various dimension of nano-confinement 7

Figure 2.1. Schematics of two-step anodization process to fabricate porous anodic aluminum oxide templates 16

Figure 2.2. SEM images of AAO templates anodized in sulfuric, oxalic and phosphoric acid electrolyte..... 18

Figure 2.3. (a) Different domain packing in isotropic and anisotropic geometries. (b) Two different types of nanopore with anisotropic geometry; trigonal and conical pores23

Figure 2.4. Schematic for the fabrication of various shape of nanopores; cylindrical, conical, truncated conical pores26

Figure 2.5. SEM images of fabricated conical pores. The depth of pore was varied by controlling the anodizing time.....28

Figure 2.6. SEM images of fabricated conical pores; (a) top-view and (b) cross-sectional view. The top diameter (D_P) of pore was varied by controlling the time for widening. All scale bar indicate 100 nm.29

Figure 2.7. SEM images of fabricated truncated conical pores with 80 nm of D_P . They have different bottom diameter (D_B) of (a) 40 and (b) 50 nm. All scale bar indicates 100 nm31

Figure 2.8. SEM images of large conical pores with 240 and 80 nm of D_P and D_B , respectively. The depth of the pores can be controlled by anodization time.....	32
Figure 2.9. Schematic for the fabrication of trigonal nanopores.	35
Figure 2.10. SEM images of triangular pores with various pore diameters. (a,b) Smaller pores were anodized at 27V and (c,d,e) larger were anodized at 140V. To vary the size of the pore, pore widening process was also performed (b,d,e).....	38
Figure 2.11. SEM images of triangular pores at different anodization times. (a) The schematic of the growth of the trigonal pores. (b) Small trigonal pores were growing as anodization time increased. (c) Large trigonal pores were growing as anodization time increased.....	39
Figure 2.12. A schematic illustration to fabricate nanostructure-patterned PUA and nanocavity-patterned PFPE regiflex replica.....	42
Figure 2.13. SEM images of fabricated nanostructure including original AAO templates, PUA 1st replica, and PFPE 2nd replica.....	43
Figure 3.1. SEM images of AAO templates from (a) top view and (b) cross-sectional view. (c) Histogram representing the distribution of diameter of AAO nanopores analyzed by image analysis software (Image J). The mean diameter of pores is 176.5 ± 5.3 nm and the length is 20 μ m. Scale bar is (a) 200 nm and (b) 2 μ m.....	53
Figure 3.2. TEM images of (a) neat SBD42 and (b) binary blends with 20 wt % hPS4.8. All of the samples are stained with OsO ₄ vapor before TEM investigation. Scale bar is 200 nm	58
Figure 3.3. TEM images of the morphology of SBD89/hPS4.5 binary blends in (a) bulk and (b) confined state by varying the weight fraction of hPS4.5. All of the samples are stained with OsO ₄ vapor before TEM investigation. Scale bar is 200 nm.	60

Figure 3.4. TEM images of the morphology of SBD89/hPS45 binary blends in (a) bulk and (b) confined state by varying the weight fraction of hPS45. All of the samples are stained with OsO4 vapor before TEM investigation. Scale bar is 200 nm.

.....62

Figure 3.5. Schematic illustration of the phase transition of SBD45/hPS45 binary blends under cylindrical confinement. (a) is the view along the pore axis and (b) is the view normal to the pore diameter. As the weight fraction of hPS45 increases, hPS is preferentially located at the center of the pore. When the weight fraction of hPS45 is further increasing, the PBD layer continuous in the pore axis is broken into droplets in order to take excess hPS chains.....63

Figure 3.6. TEM images of SBD89/hPS45 confined in cylindrical pores with different fraction of hPS45 (a,d) 0, (b,e) 20, and (c,f) 40 wt %. (a) – (c) are the views normal to the pore diameter and (d) – (f) are the views along the pore axis. All the samples were stained with OsO4 vapor before TEM investigation. Scale bars are 100 nm.....65

Figure 3.7. TEM images of SBD89/hPS with inverse structures upon molecular weight of hPS (a) 4.8k and (b) 45k hPS. (a) is normal peapod array and (b) is vesicular peapod array morphologies. All of the samples are stained with OsO4 vapor before TEM investigation. Scale bar is 200 nm67

Figure 3.8. (a) Surface energy (dispersive + polar = total) of OS as a function of curing temperature. (b) Estimated interfacial energy of PS and PMMA block on OS substrates which are cure in different temperature.....70

Figure 3.9. AFM height and phase images of SMA89 film annealed at 180 °C for 3 days in vacuum. BCP thin film was casted on the OS substrates pre-cured at different temperature.....73

Figure 3.10. The thickness of OS interlayer coated by template wetting method characterized by TEM. The thickness is 5 - 10 nm regardless of the concentration of OS solution and dip-coating times	76
Figure 3.11. TEM images of SMA89 under (a) bulk state and confined in (b) pristine cylindrical nanochannel of AAO and OS-treated AAO at (c) 300 °C and (d) 340 °C	77
Figure 4.1. Schematics for experimental procedure for characterizing morphologies of PS- <i>b</i> -PB	83
Figure 4.2. Schematic illustration of the self-assembled morphologies of lamellae-forming PS- <i>b</i> -PB under conical nano-confinement	88
Figure 4.3. SEM images of cross-sectional view of conical pores. Small and large conical pores have 80 nm (a-c) and 225 nm (d-f) of pore diameter (D_p). Both size of pores were fabricated to have various aspect ratio ($AR = h/D_p$); 2 (a,d), 3 (b,e) and 5 (c,f). Inset of the images are top-view of corresponding pores	89
Figure 4.4. TEM images of the morphology of SBL42 nanocones confined in various size of conical pores; small and large BCP nanocones with diameter of 80 nm (a-c) and 225 nm (d-f). Both small and large nanocones have three aspect ratio (h/D_p); 2 (a,d), 3 (b,e) and 5 (c,f). All of the samples were stained with OsO ₄ vapor before TEM investigation and PB block appear dark in images.	91
Figure 4.5. 3D imaging of SBL42 confined in AR3 small conical pores using TEM tomography. AAO templates is not removed. A digitally sliced electron tomography image shows the cross section of AAO templates containing BCPs parallel to the pore axis. Here, only OsO ₄ stained PB microdomains (dark region) are extracted in purple color. White arrows in magnified view indicate partially connected PB domain at the interface between polymers and pore surfaces	92

Figure 4.6. SEM images of cross-sectional view of AAO pores with different bottom shapes; small (a-c) truncated conical and (d-f) cylindrical pores. All types of pore have 80 nm of top diameter and bottom diameters were controlled to have 40 and 80 nm, respectively, which are larger than 15 nm of conical pore. All pores were fabricated to have three aspect ratio (h/D_P); 2 (a,d), 3 (b,e) and 5 (c,f). Inset of all the images are top-view of corresponding pores.....95

Figure 4.7. TEM images of the morphology of SBL42 confined within small (a-c) conical, (d-f) truncated conical, and (g-i) cylindrical pores. All of the samples were stained with OsO₄ vapor before TEM investigation. The images in yellow, blue and red box correspond to groups of stacked lamellae, mixed orientation, and concentric lamellae, respectively. (j) The schematic of comparative thermodynamic parameters and corresponding microdomain orientation depending on different shapes of the pore bottom96

Figure 4.8. TEM images of the morphology of SBL42 confined in AR3 small conical pores modified by PS-OH brush. The grafting density of PS brushes were controlled by reaction time: (a) 20 min, (b) 1, (c) 48, and (d) 120 hr. All of the samples were stained with OsO₄ vapor before TEM investigation. (e) Simulated morphologies of block copolymers as a function of interfacial energy between A blocks and confining walls ($\epsilon_{A\omega}$)99

Figure 4.9. TEM images of the morphology of SBL26 confined in small conical pores. BCP nanocones have diameter of 80 nm and various aspect ratio (h/D_P); (a) AR 2, (b) AR 3 and (c) AR 5. All of the samples were stained with OsO₄ vapor before TEM investigation.....102

Figure 4.10. Simulated morphologies of block copolymers A7B5 as functions of sizes and shapes of confining pores; (a-c) large conical pores with D_p/L_0 of 7.37 and (d-f) small conical, (g-i) truncated conical, (j-l) cylindrical pores with D_p/L_0 of 2.53. Both small and large BCP pores have three aspect ratio; 2 (a,d,g,j), 3 (b,e,h,k) and 5 (c,f,i,l). The interaction of surface is fixed at $\epsilon_{A\omega} = -0.2$ and $\epsilon_{B\omega} = 0.2$ 105

Figure 4.11. (a-c) The A-B interfacial energy (E_i), (d-f) the surface energy (E_s), (g-i) the mean-square end-to end distance of chains, and (j-l) the total free energy of block copolymers A7B5 as a function of $\epsilon_{B\omega}$. The ratio between pore diameter and repeat period (D_p/L_0) is 2.53 106

Chapter 1. Introduction

1.1. Fundamentals on Block Copolymers

1.1.1. Introduction to Block Copolymers

The control of structures with length scales from micro to molecular dimensions is crucial in progress of nanotechnology. Especially, this should be realized over length scales and dimension relevant to the specific application of interest. The organization of periodic structures with long-range order can be made by either top-down or bottom-up methods. As the top-down method, lithographic techniques such as conventional photolithography, nanoimprint lithography, e-beam lithography, and focused ion-beam (FIB) etching can produce nanoscale features even with around 10 nm linewidths in state of the art. However, these approaches are constrained by optical limit for the features produced by diffraction or by low throughput and high cost due to the sequential nature of the pattern formation. Bottom-up approaches take advantage of self-assembly of building blocks including atomic, molecular or even colloidal moieties to provide access to nanostructures with characteristic length scales of interest. Although defects in self-organization process limit the symmetries or the long range order of patterned structures, the advantages of high throughput with low-cost processing and the formation of hierarchical structures over large areas implies that at least in principle, processing methods that leverage self-assembly will have vital roles to play in the development of advanced nanotechnology.

Block copolymers (BCPs) thought of as macromolecular amphiphiles have much to offer in this context. They consist of chemically distinct homopolymers

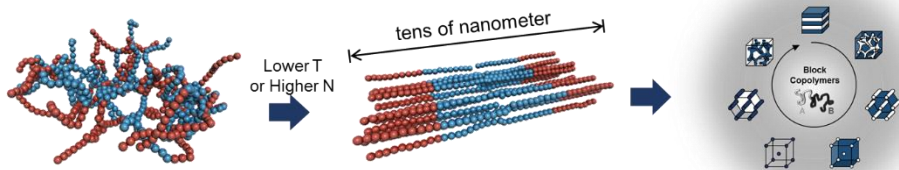


Figure 1.1. Schematic illustration of phase behavior and nanostructures of diblock copolymer depending on the volume fraction of each block.

covalently linked end-to-end as shown in Figure. 1.1.^{1,2} The self-assembly of BCPs is driven by the demixing of different polymer chains into microdomains. Since dissimilar polymer segments are physically connected, the phase separation of BCP occurs only locally and the characteristic length scale of microdomains is similar to the radius of gyration (R_g) of the polymer chains. The composition of the system is represented by the volume fraction of the constituent blocks. A generic sequence of morphologies of phase-separated BCPs is represented by the composition of the constituent blocks. As volume fraction of one block of the system is increasing, the BCPs form various structures from cubic-packed spheres through hexagonally packed cylinders, bicontinuous cubic networks and lamellae as shown in Figure. 1.1. A dissimilarity of polymer chains is represented by the Flory-Huggins interaction parameter, χ and higher temperature enhance the miscibility of the blocks. Beyond a critical temperature, the order-disorder transition temperature (T_{ODT}) the phase become thermodynamically miscible and disordered or phase-mixed melt exist. As χ is higher, the phase separation is occurred in lower temperature. Since too smaller and longer chains are difficult to be separated, the periodicities of microdomains are possible in a range of 5 to 150 nm. The development of chemistries of polymer chains makes it possible to expand a range of feasible length scales or to endow specific functionalities into the systems, such as ligand-binding capabilities or semiconducting electro-optical properties. For example, substituents on the polymer backbone can themselves assemble into ordered structures, in the case of liquid crystalline block copolymers, where order exists on ca. 0.5 – 10 nm length scales embedded within block copolymer structures on ca. 10 – 100 nm length scales. Also, complex chain architectures enable to design hierarchical nanostructures and access to unconventional morphologies.

1.1.2. Directed Self-Assembly of Block Copolymers

BCPs have a potential to design nanostructured materials and corresponding devices since two distinct blocks can be selectively treated. For example, after removing or changing one phase, BCP matrix can be used as templates for the fabrication of nanomaterials and the transfer of pattern in photolithography. BCP microdomain can also be transport media for molecules, electrons, protons, and ions, where species selectively travel in microdomains governed by the chemical identity or the size of the block. These applications are related to energy devices such as fuel cell membranes and battery separators. When the spacing of the self-assembled nanostructure is matched to exciton diffusion lengths in organic/polymer semiconductors, the optimization of the transport in heterojunction photovoltaics can be realized.

The performance of nanostructured device is sensitive to the alignment and the long-range order of the assembled morphology. For instance, the alignment of microdomains in membrane applications is important because the tortuosity of the conducting pathways should be minimized in order to optimize the transport of desire species. To enhance the performance of device using BCPs, it is of great interest to understand the interactions not only between two blocks but between blocks. The ability to direct the self-assembly of BCPs and thus dictate the desired design of effective directed self-assembly (DSA) methods and tools. There are a bunch of principal approaches for DSA of BCPs, and several contributions provide more detailed or comprehensive reviews of BCP DSA³⁻⁷ with specifically focused on thin films geometries.^{3,8-13} In general, shear¹⁴⁻¹⁹, electric^{17,20-24} and magnetic fields²⁵⁻²⁸, surface modification²⁹⁻³⁴, solvent annealing³⁵⁻³⁹, and grapho- and chemoepitaxy⁴⁰⁻⁴³ have been well investigated to control the orientation and the

defect-free pattern of BCP microdomains.

By merging self-assembly (bottom-up) with patterned template (top-down), template-assisted self-assembly (TSA) of BCP can provide rich opportunities for the development in the fabrication of devices in nanoscale, as well as fundamental studies to reveal underlying mechanism of the phase behavior of BCPs under confined environments. TSA is a process using artificial patterned templates as a grapho- or chemoepitaxy in order to control the orientation of microdomain and remove the defects of self-organized structures. While the ordering process of thin film is related to the lattice of the patterned substrate in conventional epitaxy process, templates for TSA are the topography or chemical pattern instead of the atomic lattice of the substrate to guide the assembly of the component materials. The range of characteristic lengths of templates (L_s) can be from the repeat period of BCP (L_0) to sizes much larger than that of the self-assembled materials. Recent studies have demonstrated that a various types of templates can not only control the orientation and ordering of microdomains for defect-free pattern, but induce unconventional nanostructure which have not been observed in bulk phase of block copolymers. The ability to register and control novel block-copolymer morphologies can hold a great promise in basic research of polymer physics as well as development of nanotechnologies.

1.2. Phase-Behavior of Block Copolymers under Nano-Confinement

1.2.1. Self-Assembly of Block Copolymers under 1D Nano-Confinement

When block copolymers are confined within the geometry in which characteristic length scale of template is comparable to that of polymer chains, the phase separation of block copolymer depends on not only intrinsic properties of blocks, also the interaction between the confining surfaces. The effect of confining environment can be differentiated by the direction in which the mobility of polymer chains is constraint. (Figure 1.2). In general, block polymers are confined within surfaces of constant curvature such as flat (1-dimensional, 1D), cylindrical (2D) or spherical surfaces (3D). These surfaces make the geometrical constraint at all locations within the material and break the symmetries of block copolymer's equilibrium morphology.

When block copolymers are confined within thin films, the interaction between the surface and each block and the commensurability between the characteristic length of geometries and polymer chains significantly affect the final morphologies of copolymer. In case that surfaces are attractive to one of blocks, the surfaces are wetted by that block and orientation parallel to the surfaces are formed. In contrast, perpendicular orientation is built when the surfaces are neutrally attractive to both blocks or the degree of confinement defined by film thickness (t) over the repeat period of BCP (L_0) is far from an integer. In cases where one side of film is wetted by highly attractive surface and the other side is located at air surface, a large mismatch between the film thickness and L_0 induces the quantization of the thickness of the film in which the thickness varies with position, forming hole and island to

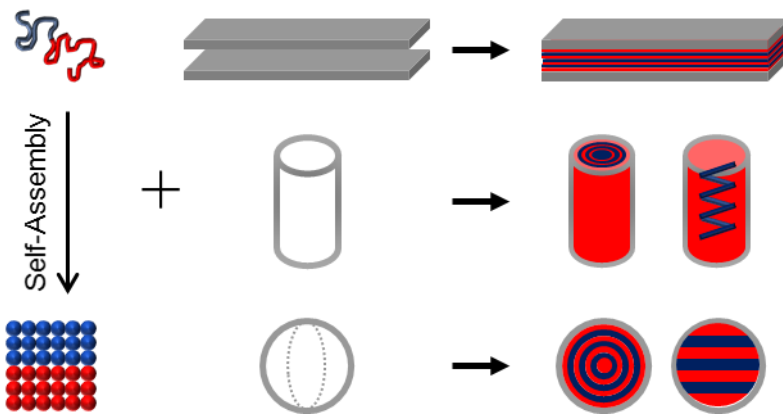


Figure 1.2. Schematic illustration of the phase behavior of diblock copolymer under various dimension of nano-confinement.

be commensurate with the repeat period of the microphase separated structure.

For applications, the surface modification to tune the interaction and relevant thickness of the film can generate targeted morphologies. Additionally, the long range order of patterned thin film can also be improved using versatile processing methods which change the geometry of boundary conditions. Graphoepitaxy is used to promote the alignment⁴⁴⁻⁴⁹, where block copolymers are confined in narrow channels which have precise integer multiples of the repeat period of the bulk block copolymer. Another way is to manipulate the thickness of BCP thin films to fabricate orientation of interest^{50,51}. Modifying the surface property of the substrate can also be introduced to tune the structures⁵²⁻⁵⁴. For example, chemically patterned substrates with periodicities close to commensurate with the L_0 of BCPs can make precisely aligned/registered nanostructures. In thin film geometry where block copolymers are one-dimensionally confined, a various of structures can be formed and controlled by tuning the energetics of interaction between substrates and materials or by controlling the boundary conditions which are well matched with the characteristic length scale of polymer chains.

1.2.2. Self-Assembly of Block Copolymers under 2D Nano-Confinement

Many studies have investigated block copolymers in 2D confined systems both experimentally and theoretically⁵⁵⁻⁶⁰. In 2D confinement, materials are constrained in two directions, mostly in xy plane, and in third dimension, geometries have comparatively infinite extent. For investigate 2D confining systems, several types of templates have been used as environments; hollow tube, porous templates and trenches. Boundary conditions of these geometries provide further symmetry constraints in the equilibrium morphology of block copolymers than 1D thin films. If the characteristic length of the confining environment is not commensurable with the repeat period of equilibrium bulk phase, the possibility of unconventional morphologies significantly increases. Experiments and simulated studies have investigated the systems with different interaction parameters and composition of BCPs. These results help to exactly predict the final morphology in any given condition of confinement even though not possible experimentally.

Moreover, in order to understand the key parameters, it is important to systematically investigate the phase behavior of block polymers under 2D confinement. For example, the structures of diblock copolymers confined within cylindrical nanopores were identified at a range of volume fractions of the minority block and degree of confinement with tuning the diameter of nanopores⁵⁵. Additionally, this work provided a good comparison of the morphologies of cylindrically confined diblock copolymers between experimentally observed TEM images and simulative results in which the effective parameters are systematically controlled⁶⁰; Since the energetic parameter for the interaction is hard to control in experiments, well-executed simulation where parameters varying correspondences to experimental situations can give a detailed information about morphologies

formed by a variety of block polymers in pores of varying diameter and affinities for each of the blocks⁵⁶⁻⁵⁹.

Under 2D confinement, incommensurability between the size of confining environment and the periodicity of polymer chain can make unconventional morphologies which have not been revealed in bulk phase or thin film. For examples, cylindrical forming block copolymers are known to make single or double helix which is coiled along the pore depth. These morphologies have huge potential applications for chiral materials that may have novel mechanical, optical or electronic properties. However, the control of handedness of helical structure should be studied further. Additionally, concentric lamellae which is commonly observed in cylindrical confinement can be used in drug delivery or photonic materials such as waveguides. To make the regularity of block copolymer pattern and the long range order of microdomain in third dimension, further development of material process should be developed.

1.2.3. Self-Assembly of Block Copolymers under 3D Nano-Confinement

Studies on 3D confined block polymers have been less exploited than other confinement systems. Based on design rules of other systems, the generalized method has been developed to control the morphologies of block copolymers as functions of structural and thermodynamic considerations. There is confining surface along each axis in 3D confinement meaning that there is frustration of the bulk behavior of copolymer chains in all directions. This give rise to either concentric structures in specific condition or the presence of defects or unrevealed structures. Specifically, when one of the block is preferentially wetted by surface with favorable interaction and the commensurability between confining geometries and polymer chains exist, block copolymer microdomains have tendency to make concentric structures. However, when surface property is neutral to both block or the symmetry between length scales are broken, unconventional morphologies are observed. In spherical confinement, the concentric wrapping of asymmetric block polymers can lead to perforated shells of the minority component pierced in a regular arrangement by structures of the majority component connecting inner and outer majority domains.

Even though much less work has demonstrated the effect of 3D confinement than 1 or 2D confinement, several studies is noteworthy as a guide line. For example, the experimental investigation of lamellae-forming block copolymers in spherical confinement was systematically studied with varying molecular weights and degrees of confinement.⁶¹ The merge of experiments and simulation to figure out the underlying mechanism for the morphologies of spherical shells of diBCP was also demonstrated.⁶² An extensive theoretical calculation even with the parameter which is hard to be realized in experiments has been accomplished to identify the

nanostructures formed by lamellar-⁶³ and cylinder-forming⁶⁴ BCPs confined to spherical geometry with controlled degrees of confinement and surface properties.

Chapter 2. Development of Anodic Aluminum Oxide Templates with Nanopores of Various Geometry for Confining Environment

2.1. Introduction

Nanostructures have been of great interests owing to their unique properties that are not shown in bulk phase or in molecular level. Many researchers have proven that nanostructures exhibit size- and shape-dependent properties.^{13,65,66} This interesting relationship has intrigued the design of more advanced materials with size- and shape-controllable nanostructures. In terms of preparing nanostructures, both top-down and/or bottom-up process such as self-assembly of materials, lithographic techniques, and template-assisted methods have been mainly introduced.⁶⁷⁻⁶⁹ Dimension of the nanomaterials such as nanoparticles (0D), nanorod/nanowires (1D), or planar sheet (2D) can be precisely fabricated on the basis of various techniques. Furthermore, the physical geometries of the nanomaterials such as not only the size of nanoparticles or the thickness of thin films but their shape can be controlled at nanoscale. This ability has enabled both detailed analysis of the materials both quantitatively and qualitatively, and thus the materials could be exploited as building blocks for much advanced materials with desired properties. For example, electronic and optical properties of metallic and semiconductor nanomaterials is strongly affected by the size of crystallite and they can exhibit quantum effect. Surface plasmon resonance (SPR) which have an interesting

behavior in sensing chemical and biological molecules is a representative example of the quantum effect.

In addition to enhanced properties, nanostructured template can be used as mold to fabricate nanomaterials with controlled dimension and as confining environment to constraint the assembly of molecules. Anodized aluminum oxide templates (AAO) consist of densely arrayed cylindrical nanopores. When the AAO is fabricated by two-step anodization method, cylindrical pores are arranged in close-packed hexagonal domain.⁷⁰⁻⁷³ The size of pore including diameter and depth can be controlled and the diameter of pores ranges from 10 to 400 nm. Even though The pores have closed ends due to Al barrier layer and the underlying Al substrate, both layers can be easily detached in order to achieve through-hole nanomembranes.

In polymer researches, Nanoporous self-ordered AAO has been used for two purposes, either as a confining environment to study the conformation of polymer chain and corresponding phase behavior under 2D confinement or as nanostructured templates to fabricate polymeric nanostructures such as nanotube and nanorod. As porous templates, AAO membranes present distinctive features different from other templates regarding the fabrication of polymer nanostructures. Firstly, AAO templates have a wide range of structural feature regarding pore diameters, pore lengths and interpore distances and this benefits to make polymer nanomaterials with tailored structures. Also, cylindrical nanopores are monodispersed in shape and size and arrayed in hexagonally packed patterns, allowing the replication of ordered nanostructures with uniformity. Additionally, template-assisted fabrication techniques have been well investigated so far and the patterning process is possible in either condition molten or solution process.⁷⁴ After replicating, to obtain free polymer nanostructures, Al and AAO layer can be easily removed by acidic or basic

etchant without damage to the polymeric domain.

AAO is one of the main tools to demonstrate confinement effects on the phase behavior of polymers. Cylindrical nanopores with a diameter compared to polymer chain length can impose 2D spatial confinement. The easiness to control pore diameter is advantages in manipulating the degree of confinement defined by the ratio between characteristic length of confining geometries and embedded materials. Also, the uniformity of the pore structures can make well-defined geometries which is crucial to precisely investigate the effect of confinement. another advantages of AAO is thermal and mechanical stability in the temperature ranges and thermal process such as crystallization, melting, molecular dynamics and order–disorder transitions can be identified.

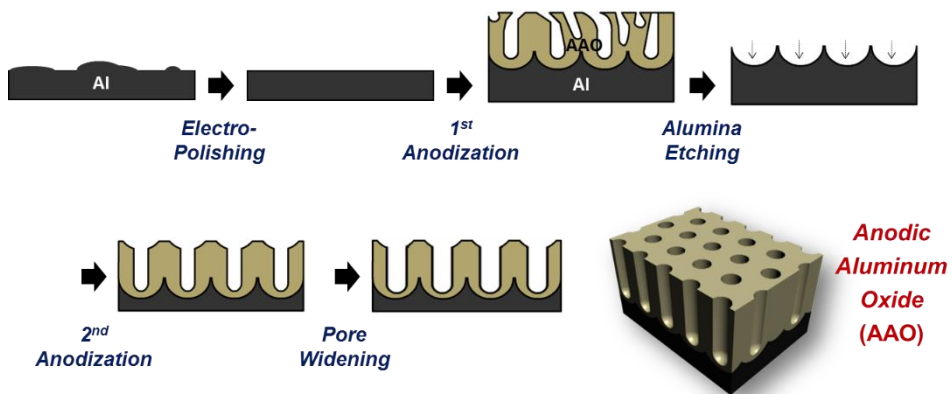


Figure 2.1. Schematics of two-step anodization process to fabricate porous anodic aluminum oxide templates.

2.2. Effect of Asymmetric Geometry on Confined Self-Assembly

2.2.1. AAO Templates with Cylindrical Nanopores

Anodized aluminum oxide (AAO) drew the attention in the nanotechnology field, when Masuda and co-workers reported two-step anodization process for self-ordering of pores⁷² and the subsequent development of a method for achieving ordered AAO templates. (Figure 2.1)⁷⁵ Two separate electrochemical oxidations consecutively works over the surface of aluminum foil. Briefly, a high purity aluminum foil is first cleaned and electro-polished. Then, 1st anodization is performed in an acidic electrolyte under constant voltage which make not ordered porous oxide structures. In contrast to disorder top surface, oxide-aluminum interface has hexagonally arranged hemispherical concave pattern. After removing out oxide layers, during 2nd anodization reaction, the current is concentrated on the pit of concaves and it works as nucleation points where the hexagonally ordered pore structures grow. After pores with desired length were achieved, pore diameter can be widened by post-etching process which can selectively dissolves the pore wall radially.

The dimensions of the structural features in AAO will determine the dimensions of the replicated polymer nanostructure when used as a template. Therefore, dimensions of the original template impact directly on the properties and functionality of the polymer nanostructure. Likewise, pore dimensions define the degree of spatial confinement experienced by the polymer material when used as a confining medium. Hence, the great importance of size control in nanoporous AAO templates. The characteristic dimensions of pore structure in a self-ordered AAO

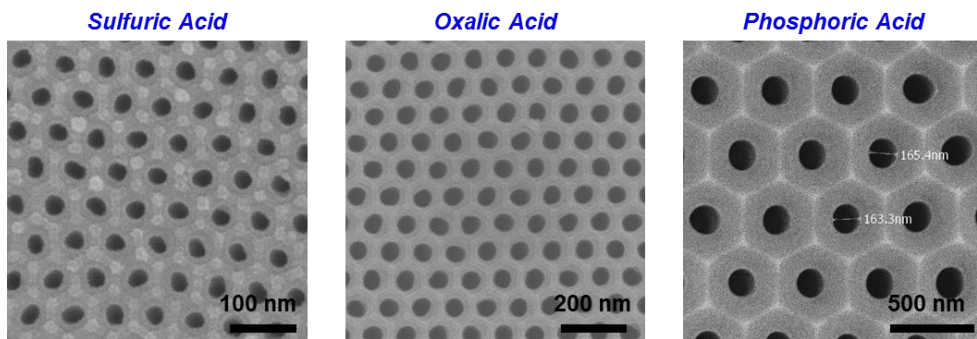


Figure 2.2. SEM images of AAO templates anodized in sulfuric, oxalic and phosphoric acid electrolyte.

Electrolyte	Voltage (V)	Interpore Distance (D_{int}) (nm)	Pore Diameter (D_p) (nm)
Sulfuric Acid	25	40, 60	20 – 50
Oxalic Acid	40	100	40 – 80
Phosphoric Acid	195	500	100 – 400

Table 2.1. Pore dimension including interpore distance (D_{int}) and pore diameter (D_p) depending on the type of electrolytes and output voltage for anodization.

template can be defined in terms of pore diameter, pore length and interpore distance (lattice constant of the hexagonal symmetry). These can be easily tuned by applying the appropriate set of reaction parameters during the anodization, namely constant output voltage, anodization length, temperature, stirring and nature and concentration of the electrolyte. It is well known that the interpore distance is linearly proportional to anodizing potential.⁷⁶ So far, a few self-ordering regimes have been identified under mild anodizing (MA) conditions as shown in Figure 4.2 and Table 4.1. Also, Lee et al. recently discovered that a routinely employed industrial process using high current densities, the so-called hard anodization (HA), enabled AAO templates with interpore distance between 220 and 300 nm⁷⁷, a range not covered by MA self-ordering regimes.

Pore diameter is also linearly proportional to the applied potential. However, whereas the interpore distance, and the related pore ordering, is established during the first anodization, and is fixed for each value of applied voltage, the diameter of pores can be further adjusted in a third step of the fabrication process. In this third step, the originally obtained pores are enlarged by the controlled dissolution of the pore walls using acidic solutions (typically H₃PO₄ solutions). Thereby, through the selection of the appropriate anodization parameters and subsequent pore widening process, one can cover almost the entire range of diameters from 10 to 400 nm. The second anodization step also allows precise control over the length of the nanopores from tens of nanometers up to hundreds of microns.

2.2.2. Effect of Asymmetric Geometry on the Self-Assembly of Block Copolymers

Anisotropy and asymmetry in nanostructures have been reported to influence optical properties and adhesion properties, respectively.^{78,79} Triangular Au or Ag nanoparticles have been proved to enhance plasmon resonance by localizing the incoming light to the sharper corners of the structures. Arrays of nanorods bent to a direction were confirmed to be useful as physical adhesive. Therefore, there are many other structural parameters to influence physiochemical behavior of nanomaterials besides their dimensions or sizes. The various parameters have open up possibilities to create more advanced materials having specifically manipulated properties. This implies that finding of new structural parameters in nanostructures should be urged to develop academic research in nanoscience and meet applicability of the materials in industries.

Herein we, based on the interesting structural parameter, exhibited the importance of our finding to control the physical structuring of organic and inorganic materials. We introduce another structural parameter to help understanding of nanomaterials. From a self-assembled structure, we adopted nanoscopically anisotropic geometries with regularly packed structure. Different from isotropic geometries such as cylindrical channel, thin film, or sphere, anisotropic geometries break the symmetry of molecular packing under confinement and the frustration of assembled molecules are maximized in a singularity point (i.e. vertices, tip) (Figure 2.3a) This can lead to unconventional assembly of chained molecules and novel nanostructures which is not observed.

With engineering the synthetic method, anisotropy in two different plane was demonstrated. Specifically, trigonal pores have anisotropy in XY-plane and conical

pores in z-axis (Figure 2.3b). Among the self-assembled molecules, block copolymers are significantly affected by confinement due to their connected structure and immiscibility. Since the conformation of chained molecules cannot be stretched or compressed over certain size in entropic point, morphological transition occurs to compensate the loss of conformation entropy within vertices or tips. From this perspective, we investigated the phase behavior of block copolymers within anisotropic geometries and try to find out the way to release entropic penalty of polymer chains.

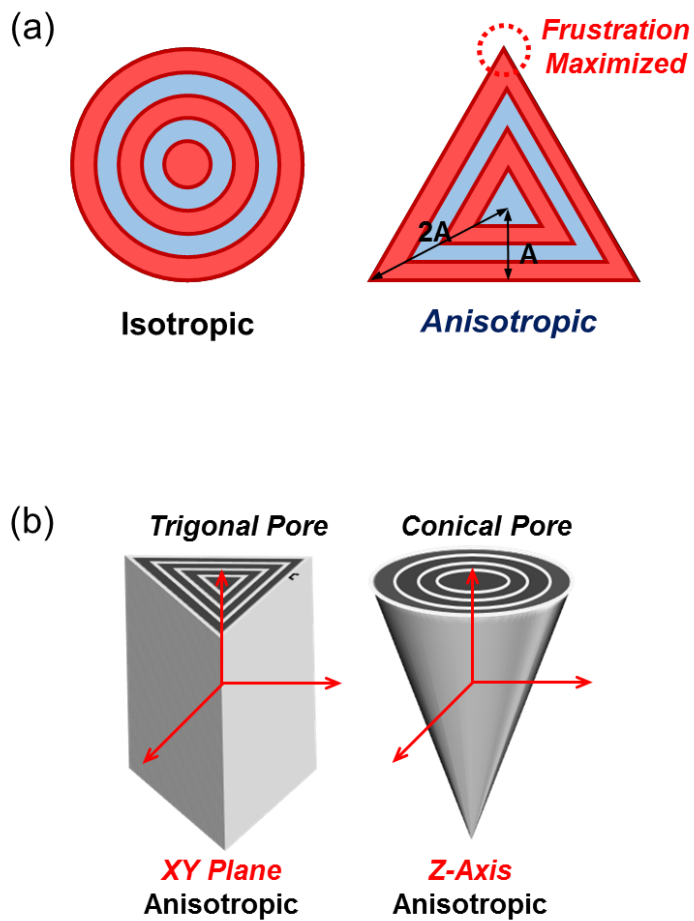


Figure 2.3. (a) Different domain packing in isotropic and anisotropic geometries. (b) Two different types of nanopore with anisotropic geometry; Trigonal and conical pores.

2.3. Development AAO Templates with Conical Nanopores

2.3.1. Experimental

Materials A high purity aluminum foil (99.999 %) with 0.5 mm thickness were purchased from Good Fellow, UK and used after degreased in acetone and isopropanol solution. 70 % Perchloric acid, oxalic acid, 85 % phosphoric acid, ethanol, toluene was purchased from Sigma-Aldrich and used as received.

Fabrication of AAO Templates The schematics for the fabrication of AAO templates was described in Figure 2.4. The aluminum slice was electropolished at 20 V in 70 % perchloric acid (HClO₄, Aldrich) and ethanol (C₂H₅OH, Aldrich) mixture (v/v = 1:4) at 5 °C for 5 min. Although both small (pore diameter, $D_p = 80\text{nm}$) and large ($D_p = 240\text{ nm}$) conical pores were fabricated by the two-step anodization process, the anodizing condition was different to control pore diameter and interpore diameter; mild and hard anodization.⁸⁰⁻⁸³ For large one, the electropolished aluminum plates were anodized at 140 V in 0.3 M oxalic acid solution at 0 °C for 2 hr, followed by chemical etching of aluminum oxide layer in an aqueous solution of phosphoric acid (6.8 wt %) and chromic acid (1.8 wt %) at 70 °C for 6 hr. Then, second anodization (122 V, 10 °C) and pore widening were alternatively repeated to obtain desired aspect ratio and pore diameter. Reaction time and the number of repetitions was determined to make smooth inner surface of the pores. To make conical pore with a smaller diameter, polished aluminum sheet was anodized at 40 V at 15 °C for 12 hr. After removing out alumina layer, the recursive process of anodization and pore widening was carried out at the same condition as first anodization. The pore widening process was conducted in an aqueous phosphoric acid solution (4.0 wt %) at 30 °C. To examine the effect of curvature at the bottom, truncated conical pores and cylindrical

pores were also prepared. To make truncated conical pores, pre-made conical pores with 60 nm diameter were widened for 20 min. The depth (h) of pores was controlled to have an aspect ratio (h/D_p) of 2,3 and 5. The detailed information of prepared nanopores including the diameter (D_p), the radius of curvature at the bottom (r_c), and aspect ratio ($AR = h/D_p$).

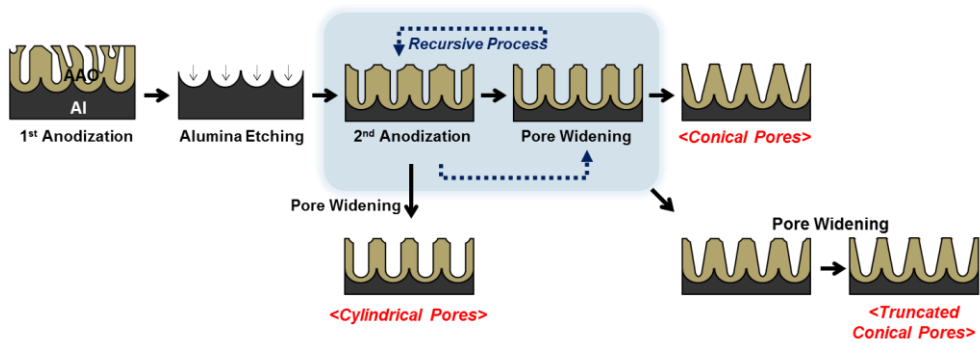


Figure 2.4. Schematic for the fabrication of various shape of nanopores; cylindrical, conical, truncated conical pores.

2.3.2. Results and Discussion

We prepared conical pores which have tapered pore diameter along z-axis via recursive process of anodization and pore-widening step. By manipulating either step, the depth and diameter of pores could be controlled. For deeper pore, the total time for anodization should be increased and we increased the number of recursive cycle instead of the time for anodizing reaction. If only reaction time increase in a hold of the number of cycles, the edge resulted from alternative process could be made. As a result, conical pores with various depth were fabricated. (Figure 2.5). As shown in images, all the pores had smooth inner surface which would not affect the phase-behavior of confined molecules. The pore diameter of conical pores was also controlled by varying the time for pore-widening step (Figure 2.6). As the time for anodization maintained, the etching time for widening was only varied. With smaller time, smaller diameter of pore was achieved. Since the variation in pore size could be different degree of confinement, it is important to demonstrate the sensitivity of controlled process. In this experiment, the temperature of each step was lower than the conventional method in order to tune the size more accurately.

Conical pores with smaller diameter than 80 nm gave a new pathway to fabricate truncated conical pores. Since outer wall of AAO templates vulnerable to etching solution (phosphoric acid) can be etched out to make 80 nm of diameter as maximum, conical pore with fully widened diameter cannot be widened more. However, diameter less than 80 nm still have enough space for widening and pre-made conical pore can be more etched out radially including the bottom of the pores. Thus, post-widening can make larger bottom diameter, resulting in truncated conical pores. The bottom diameter (D_B) also can be varied even with same top diameter (D_P). Figure 2.7 shows that two different pore with 80 nm of D_P have 40 and 50 nm

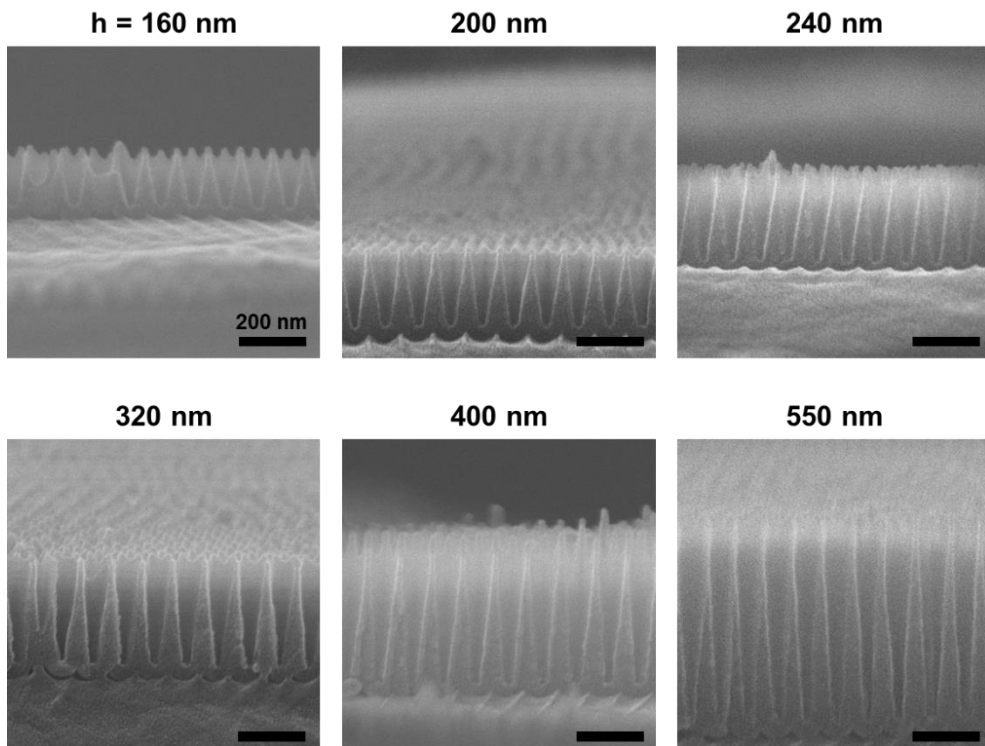


Figure 2.5. SEM images of fabricated conical pores. The depth of pore was varied by controlling the anodizing time.

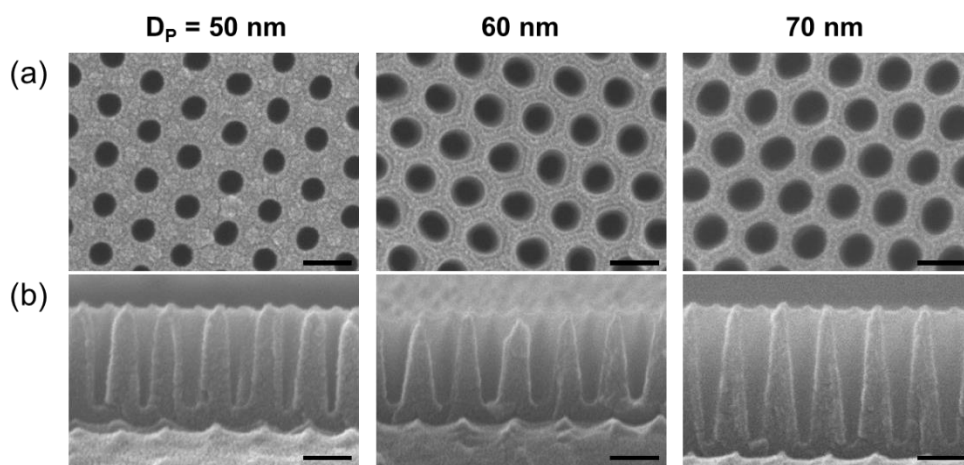


Figure 2.6. SEM images of fabricated conical pores; (a) Top-view and (b) cross-sectional view. The top diameter (D_p) of pore was varied by controlling the time for widening. All scale bar indicates 100 nm.

of D_B . To prepare truncated conical pores with different D_B , pre-made conical pore with 60 and 50 nm of D_P was widened to 80 nm. Since the bottom area (i.e. the tips of conical pores) could be a singularity for severe confinement, the variation could be used to investigate the effect of vertices.

Finally, we also tried to make another conical pores with different interpore distance and bottom diameter. For templates not only confinement but fabrication of nano-materials, the dimension of geometry is important. For example, the optical response in anti-reflective coating is significantly affected by the scale of patterns such as the size and the period.^{84,85} Since, with mild anodization process, the period and size of the nanopores are limited to a few cases, we adopted hard anodization method to make larger conical pores and details are described in experimental section. Figure 2.8 shows SEM images of conical pore with 240 and 80 nm of top and bottom diameter (D_P and D_B). Compared to smaller cone, the dimension including the radius curvature at the bottom was increased in triple and the interpore distance was also changed to have 300 nm. The feasibility to control the size and shape of nanopores enables to develop relevant research such as the self-assembly under confinement or patterning the materials for optical applications. This results will be discussed in later section.

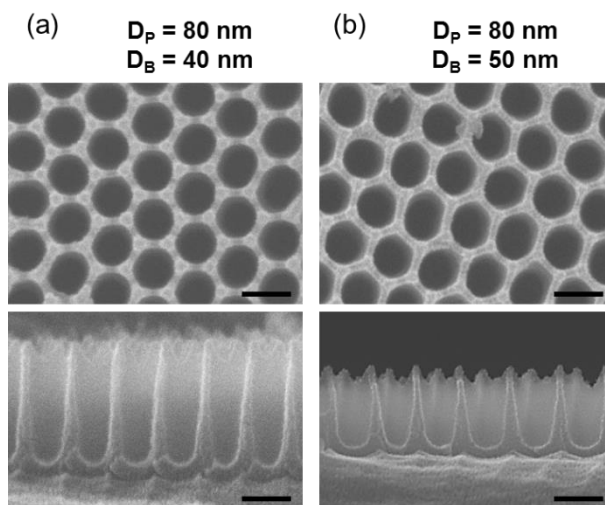


Figure 2.7. SEM images of fabricated truncated conical pores with 80 nm of D_P . They have different bottom diameter of (a) 40 and (b) 50 nm. All scale bar indicates 100 nm.

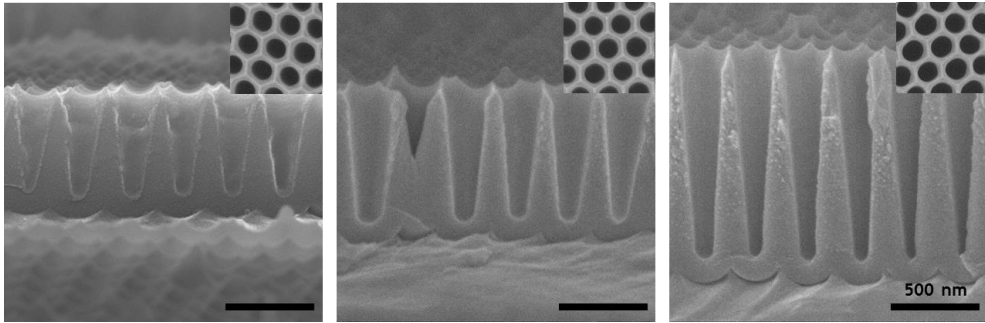


Figure 2.8. SEM images of large conical pores with 240 and 80 nm of D_P and D_B , respectively. The depth of the pores can be controlled by anodization time.

2.4. Development AAO Templates of Trigonal Nanopores

2.4.1. Experimental

Materials A high purity aluminum foil (99.999 %) with 0.5 mm thickness were purchased from Good Fellow, UK and used after degreased in acetone and isopropanol solution. Ether-terminated PDMS, (3-aminopropyl)triethoxysilane (APTES), 70 % perchloric acid, oxalic acid, 85 % phosphoric acid, ethanol, toluene was purchased from Sigma-Aldrich and used as received.

Fabricate Concave Pattern on Al Substrates The schematics for the fabrication of AAO templates was described in Figure 2.9. The aluminum slice was electropolished at 20 V in 70 % perchloric acid (HClO₄, Aldrich) and ethanol (C₂H₅OH, Aldrich) mixture (v/v = 1:4) at 5 °C for 5 min. Polished slice was anodized in 0.3 M oxalic acid at 40 V and 15 °C for obtaining 100 nm spacing pattern or in 0.1 M phosphoric acid at 195 V and 0 °C for 500 nm spacing pattern. Selective etching of the ordered alumina layer in an aqueous solution of phosphoric acid (6.8 wt %) and chromic acid (1.8 wt %) at 70 °C for 6 hr remains aluminum substrates with hexagonal packing concaves pattern.

Replicate Convex Pattern from Al Substrates To replicate the concave to convex pattern, 0.5 ~ 2 um thick Al was deposited on the concave pattern using e-beam evaporator. For an ease of detachment between them, anti-adhesion surface treatments at the surface of pre-made concave pattern are performed before metal deposition.⁸⁶ Briefly, oxygen plasma-treated Al slice was dipping in APTES solution (1 wt% in methanol) for self-assembled monolayer of APTES and washed out excess molecules. Ether-terminated PDMS was casted on APTES and heated at 80 °C for 4

hr to link amino group of APTES to ether group of PDMS, followed by washing out unreacted PDMS.

The evaporated Al with convex patterns in inverse hexagonal packing was detached as supported by a substrate with a thin adhesive layer. The convexly patterned Al foils were anodized under modified conditions; 0.1M H₃PO₄ at 140 V for 500 nm spacing pattern and 0.1M H₃PO₄ at 27 V for 100 nm spacing pattern. As cylindrical or conical pores, as-anodized pore arrays were immersed in 0.1M H₃PO₄ at 30 °C at different time scales to obtain triangular with various pore sizes.

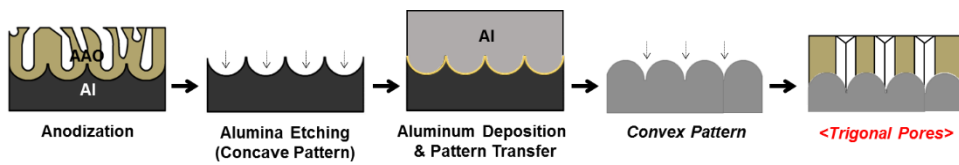


Figure 2.9. Schematic for the fabrication of trigonal nanopores.

2.4.2. Results and Discussion

As the sharp peaks in the original concave patterns become the lowest depressions in the replicated convex pattern, the packing structure of the pits were opposite to each other: hexagonal packing in the concave patterns and inverse-hexagonal packing in the convex patterns. As electric field is distributed vertically to the surface, field distribution on rough or patterned surface should change locally. In that aspect, electric field distribution for pore growth during anodization is anticipated to be more concentrated in the lower depression of each pattern where pores are anticipated to grow. Therefore, pores grown from each pattern should also exhibit the opposite packing structures. Furthermore, pore shape will be determined to minimize the mechanical stress in pore growth based on the basis of the imposed patterns.

As reported in other studies, interpore spacing (D_{int}) are determined by output voltage (U_{anod}) for constant voltage condition.⁸⁷ The equation 1 represents the linear relationships between D_{int} and U_{anod} .

$$D_{\text{int}} = - 1.7 + 2.81U_{\text{anod}} \quad (1)$$

However, this relation is only applied for the convex patterns where the distance between pores is regular. There are three different pit spacing in the unit structure of the convex patterns: $1/2 D_{\text{int}}$, $\sqrt{3}/2 D_{\text{int}}$, and D_{int} , where D_{int} indicates the pit spacing of mother concave pattern. Hence, anodization for the convex Al was performed under modified conditions from concave Al. The optimal condition was found in the middle of the voltages corresponding to $1/2 D_{\text{int}}$ and D_{int} as demonstrated in other studies.^{88,89}

By anodizing the convex patterned Al, interesting results in pore shape and its ordering was observed. Triangular pores with high degree of anisotropy were grown

from the convex Al (Figure 2.10). In previous studies making non-circular pores, the anisotropic pore shape was only achieved by fully etching the pores until the frame of the pores barely remains.⁸⁸ However in this study, we fabricated well-defined triangular pores with sharp corners as they are synthesized. With pore-widening process, triangular pores which sizes are tunable in a wide range were also demonstrated. Figure 2.10 exhibits that the triangular pores are tunable in their size ranging from a few tens of to a few hundreds of nanometers. Even though the vertices of triangle were covered by dome shaped wall, they could be identified by the pattern imprinting of polymers.

The depth of trigonal pores was also controlled until the deposited Al is used up. Figure 2.11 shows time-dependent growth of trigonal pores. As anodization was working, the electric field was concentrated on the pit of convex pattern and trigonal pores was growing (Figure 2.9a). Both small and large pores could be anodized and aspect ratio of pore could be reach to 10.

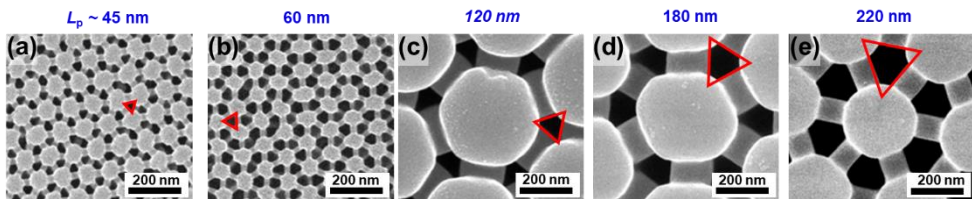


Figure 2.10. SEM images of triangular pores with various pore diameters. (a,b) Smaller pores were anodized at 27V and (c,d,e) larger were anodized at 140V. To vary the size of the pore, pore widening process was also performed (b,d,e).

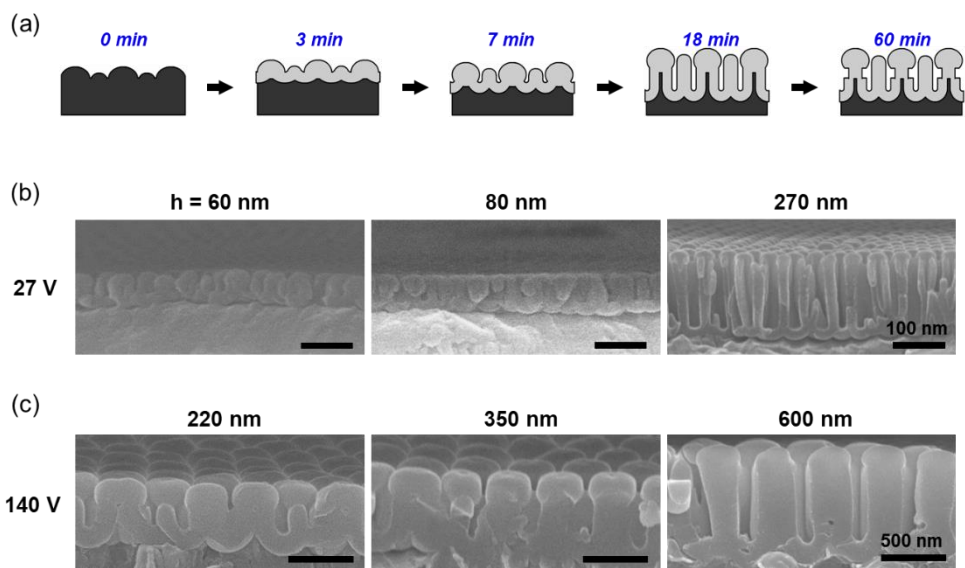


Figure 2.11. SEM images of triangular pores at different anodization times. (a) The schematic of the growth of the trigonal pores. (b) Small trigonal pores were growing as anodization time increased. (c) Large trigonal pores were growing as anodization time increased.

2.5. Pattern Transfer of Ordered Nanostructures

2.5.1. Experimental

Surface Modification of AAO Template Porous AAO templates with conical and trigonal pores were fabricated as described previous sections. For an ease to release the polymeric replica molds from AAO templates, a surface modification of AAO template was conducted. The surface of the AAO templates was treated with anti-adhesion layers as detachment of deposited Al layer in section 2.4.

Preparation of Rigiflex Replica Molds Nanocone or nanoprism-patterned PUA replica molds were prepared from AAO templates by dispensing PUA (311RM, Minuta Tech.). After UV exposure through transparent poly(ethylene terephthalate) (PET) film used as adhesive fixture, the PUA replica was gently detached from the surface-modified AAO templates. Further UV exposure was conducted for 3 hr to fully cross-link the precursors. PFPE mold which had conical or trigonal pores as AAO templates were prepared by patterning PUA mold. PFPE (MD700, Fluorolink) prepolymer mixture was dispensed onto the first PUA replica mold. After UV curing, nanocavity-shaped PFPE replica mold could be detached from PUA mold. The schematics of replication was illustrated in Figure 2.12. All nanostructures were characterized by a field emission-scanning electron microscope (FESEM, JSM-74F).

2.5.2. Results and Discussion

Figure 2.13 is the Minuta Tech.). After UV exposure through transparent poly(ethylene terephthalate) (PET) film used as adhesive fixture, the PUA replica mold was fabricated. The advantage of using rigiflex replica molds is the self-replication of molds with sub-100 nm features. A negative-type PFPE replica mold featuring nanocavities was realized by a two-step replication from the original AAO template (Figure 2.11), allowing the fabrication of nanostructures of different materials. A poly(urethane acrylate) (PUA (311RM), Minuta Ltd.)⁹⁰ nanocone/nanoprism replica mold was prepared by the UV crosslinking of the liquid prepolymer dispensed into an AAO template. After detaching the cured PUA replica mold from the AAO template, we exposed the replica mold to UV for the complete crosslinking of the replica mold. Then, PFPE precursors (MD700, Fluorolink) were deposited onto the first PUA replica mold. The UV crosslinking and detachment of PFPE from the first replica mold resulted in the second PFPE replica mold with nanocavities. Likewise, the second PFPE replica mold has served as the template to prepare different nanostructures with another material which has optical or conductive functionality.

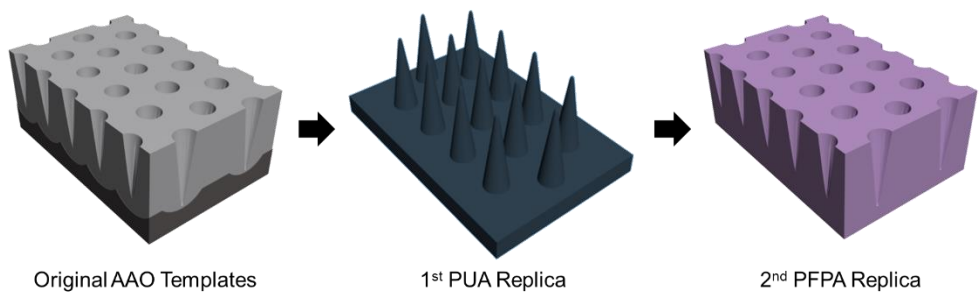


Figure 2.12. A schematic illustration to fabricate nanostructure-patterned PUA and nanocavity-patterned PFPE regiflex replica.

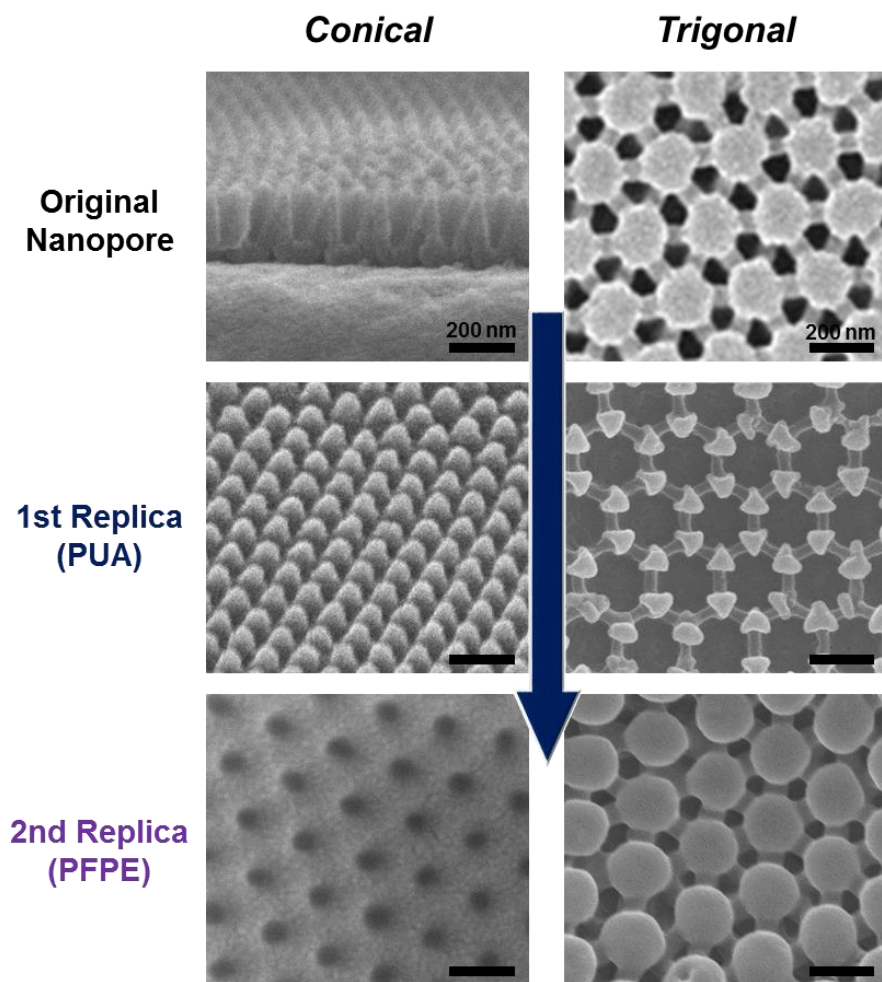


Figure 2.13. SEM images of fabricated nanostructure including original AAO templates, PUA 1st replica, and PFPE 2nd replica.

2.6. Conclusion

We fabricated various size and shapes of nanopore which can be used as confining environment and template for the synthesis of nanomaterials. First, by manipulating anodization process, conical and truncated conical pores were achieved. The tip of the nanocone is important because it can induce electrical or optical enhancement and be used as anisotropic geometries for nano-confinement.

Also, we found inverse-hexagonal packing structure from self-assembled nanoporous AAO via simple replication process. Exploitation of the finding enabled us to fabricate both triangular and circular pores from the identical patterns with the opposite curvatures. Differently from other studies adopting the same pit ordering, the pores we manufactured in this study presented better-defined triangular feature. We explain that the greater anisotropy in pore shape comes from the topography of the pattern as well as the pit ordering structure. By replicating the pore structure, we found that the corners of the triangles kept sharp up to the aspect ratio of 6.5. Therefore, the triangular pores by our method were shown to be a good candidate as a template for making non-circular nanorod arrays.

Lastly, we presented a strategy for a low-cost fabrication process of ordered nanostructures by employing a direct transfer method using a rigiflex and reusable replica mold obtained from AAO template. The low surface energy as well as the strong resistance to common organic solvents of the PFPE replica molds allowed easy and successful transfer of nanostructure onto target substrates. Consequently, this new patterning process demonstrates, the possibility to reproducibly prepare well defined ordered nanostructures using reusable PFPE molds and also to effectively eliminate potential ionic impurities commonly caused by the direct dissolution of AAO or Si templates, which would deteriorate the device performance.

Chapter 3. Morphological Transition of Block Copolymer within Cylindrical Channels

3.1. Introduction

The self-assembly of block copolymers (BCPs) has been highlighted in both experimental and theoretical investigations due to their ability to generate self-organized periodic nanostructures over large scale.^{1,2} BCPs consist of chemically distinct homopolymer chains covalently linked together at one end. The simplest BCPs, linear diblock copolymers can form microphase-separated morphologies including spheres, cylinders, lamellae, and gyroids depending on volume fraction, chain length and interaction parameter of copolymer chains. There have been long standing interests in utilizing external fields to direct the self-assembly of BCPs, which has the potential for further expanding the fabrication of novel nanostructures.^{16,28,31,39,44,91-93} In particular, template-assisted approaches have been employed to engineer polymeric particles with controllable shape and structure. It has been shown that the self-assembly of block copolymers (BCPs) in 2D confined space is a robust and facile technique to create novel BCP nanostructures that are not available in bulk state.⁹⁴⁻⁹⁶ Since the confining walls constraint the copolymer chains only radially, the degree of confinement can be defined as the ratio between the diameter of pores (D) and the characteristic length (L_0) of copolymer chains. Depending on the commensurability (D/L_0) and interfacial interactions, a variety of morphologies such as concentric ring, stacked disk or torus, multiple helices and peapod arrays have been achieved.⁹⁴ Controllable shape, size, internal structure and

surface topology of self-assembled BCPs play a significant role in applications such as photonic crystals, optical sensors and organic devices.⁹⁷⁻⁹⁹

The morphology of mixture of BCPs and corresponding homopolymers (i.e. AB/A or AB/A/B) has been well explored up to now.¹⁰⁰⁻¹⁰² Researchers have introduced homopolymers in BCP processing to extend the study beyond the morphological behavior of BCPs. The phase behavior of BCP/homopolymer blends is more delicate than that of pure block polymers, since there are intricate interplays of two kinds of phase transitions; microphase and macrophase transition. When a small amount of A homopolymers is added to AB block copolymers, BCPs easily accommodate homopolymer chains within microdomains of A block. As the amount of added homopolymers increases, a solubility limit of homopolymer in BCP microdomain is reached and macrophase separation eventually occur. The solubility limit is determined by the relative chain lengths of homopolymer and corresponding block in BCPs as well as the total volume fraction of A polymers in the blends.^{102,103} Various phase transitions of BCP microdomains have been demonstrated depending on the molecular weight and composition of homopolymers added.

In addition, homopolymers were also used to fill the defect-prone region in BCP microdomains that otherwise highly stretched copolymer segments would occupy.¹⁰⁴⁻¹⁰⁶ Since chain conformation of BCPs under confinement is severely restricted by the geometric factors (i.e. commensurability and curvature), adopting homopolymers within BCP self-assembly under confinement could significantly alleviate the stress of confined copolymer chain by filling in the high-stress region. Previously, the phase behavior of binary blends of diblock copolymer/homopolymer under 3D confinement was studied both experimentally and in simulation.^{107,108} Recently, Xu et al. described the structural transformation of BCP/homopolymer

assemblies under cylindrical confinement with homopolymers added.¹⁰⁹ However, this work only identified the change of BCP nanostructure but did not clarify the underlying mechanism of the phase transition in the mixtures of BCP and homopolymer.

Along with blending with additional molecules, the phase behavior of block copolymers under nano-confinement can be controlled by surface treatment. Since, in confined state, polymer chains are neighbored with both other chains and substrate, the effect of interfacial energy between substrate are significantly increased. Previous works demonstrated that the orientation of block copolymers thin film could be controlled by various surface treatment method.¹¹⁰⁻¹¹² Mansky et al. demonstrated that random copolymer brush could induce neutral wetting behavior of block copolymer chains which had same consisting block as random copolymers. Also, Suh et al. reported that the orientation of BCPs can be controlled by organosilicate interlayer which had tunable surface energy upon curing temperature. While the modification of surface energy of substrate was well established in thin film geometries, same approach under 2D confinement have not been studied yet. Within cylindrical nanochannel, polymer chains are totally enclosed by the wall of substrates and the influence of interfacial energies are much enhanced compared to thin film geometries.

In this report, we studied the phase transition behavior of block copolymers using two different methods: addition of homopolymer and surface treatment using organosilicate. Firstly, Block copolymer/homopolymer binary blends in cylindrical confinement was investigated in comparison with that in the bulk state. The phase behavior of lamellae-forming poly(styrene-*b*-1,4-butadiene) (PS-*b*-PB) in both bulk and 2D confinement were examined with different chain length and weight fraction

of homopolymers. Specifically, while low molecular weight hPS generally prefers dissolution into BCP microdomains with more curved interfaces, hPS with high molecular weight leads to the microemulsion phase. By the comparative study of bulk and confined states, we conclude that the effect of hPS addition on the phase transition of BCP was significantly enhanced in the nanoscale 2D confinement compared to the bulk state. Constraints caused by confinement make the phase transition of BCPs more sensitive to the addition of homopolymers, and at the same time the homopolymer chains relieve the stress which copolymer chains experience under confinement.

Secondly, we changed the surface properties of AAO templates via organosilicate (OS) interlayer coating. In nanometer scale 2D confinement, the phase behavior of BCPs is mainly dependent upon commensurability and interfacial interaction. However, most studies have focused only on the effects of commensurability on the microdomain of BCP. Here, we employed organosilicate which has tunable surface energy upon curing temperature as interlayer to examine the phase behavior of BCPs as a function of interfacial energy.^{31,112} The OS interlayer was coated on inner surface of anodized aluminum oxide (AAO) pores by template-wetting method and cured in a range of temperature to control the surface energy of interlayer. Lamellae-forming poly(styrene-*b*-methyl methacrylate) (PS-*b*-PMMA) (SMA) was injected in the OS-coated AAO pores in the melt by capillary forces. With detailed analysis, we could identify that the self-assembly of SMA in 2D confinement is competitively affected by entropic and enthalpic effects as interfacial energy is changed. As simply controlling the curing temperature of OS interlayer, various morphologies arising from both the preferential wetting behavior and neutral wetting behavior were identified. This work provides the proof-of-principle of

microdomain transitions in self-assembled BCP under cylindrically confined geometry.

3.2. Experimental

3.2.1. Block Copolymer/Homopolymer AB/A Binary Blends within Cylindrical Channels

Materials Diblock copolymers PS45k-*b*-PB44k (SBD89, $M_w/M_n = 1.04$), PS20k-*b*-PB22k (SBD42, $M_w/M_n = 1.03$), homopolymers hPS 4.5k (hPS4.5, $M_w/M_n = 1.07$) and hPS 45k (hPS45, $M_w/M_n = 1.04$) were purchased from Polymer Source, Inc., Canada. The repeat periods (L_0) of SBD89 and SBD42 were 42 and 30 nm, respectively. Detailed information including volume fraction of PB block (f_{PB}) in SBD/hPS binary blends is listed in Table 3.1.

AAO templates were fabricated by the two-step anodization process.^{83,113,114} First, a high-purity aluminum foil (99.999 %, 0.5 mm thick, Good Fellow) was degreased in acetone and isopropanol solution. Subsequently, the aluminum slice (2 x 5 cm) was electro-polished in a perchloric acid (HClO₄, Aldrich) and ethanol (C₂H₅OH, Aldrich) mixture (volume ratio = 1:4) at 20 V. The polished aluminum sheet was then anodized at 195 V in 0.1 M phosphoric acid solution maintained at 0 °C for 9 hr. After the first anodization, the aluminum oxide layer was chemically removed by etching in an aqueous solution of phosphoric acid (6.8 wt %) and chromic acid (1.8 wt %) at 60 °C for 8 hr. Finally, the second anodization was conducted at the same condition as the first one for 3 hr to produce 100 nm diameter pore with a length of 20 μm. To obtain 170 nm pore diameter, the pore widening was performed in aqueous phosphoric acid solution (10 wt %) at 30 °C for 25 min (Figure 3.1).

PS-*b*-PBD and PS Homopolymer Blends inside AAO Templates PS-*b*-PBD and hPS with different weight fractions of hPS ($\omega_{hPS} = m_{hPS}/(m_{hPS} + m_{SBD})$) were

dissolved in toluene at a concentration of 2.0 wt %. 0.2 ml of polymer solution was 24 hr and annealed under vacuum at 125 °C for 7 days. Aluminum layer and casted onto a clean AAO template (1 × 1 cm) and polymer blends entered the AAO pores. After solvent evaporated slowly, it was completely dried in a vacuum oven for alumina were then removed in copper chloride (CuCl₂)/hydrochloric acid (HCl) solution and 5.0 wt % sodium hydroxide (NaOH) solution, respectively. To prepare the samples for TEM characterization, free-standing SBD/hPS nanorods were first stained with an aqueous solution of osmium tetroxide (OsO₄) and embedded in an epoxy resin composed of Embed 812, dodeceny succinic anhydride (DDSA), nadic methyl anhydride (NMA) and DMP-30 (Ted Pella). After curing at 60 °C for 24 hr, the epoxy-embedded samples were then cut with a diamond knife into 70 nm thin sections using a Leica Ultramicrotome.

Sample Name	BCP	Molecular Weight (g/mol)	Homo-polymer	Molecular Weight (g/mol)	Weight Fraction (ω) ^a	f_{PB} ^b
SBD42	PS- <i>b</i> -PB	20k- <i>b</i> -22k			0	0.55
SBD89	PS- <i>b</i> -PB	45k- <i>b</i> -44k			0	0.52
SBD42/S4.8_0.2	PS- <i>b</i> -PB	20k- <i>b</i> -22k	PS	4.8k	0.2	0.44
SBD89/S4.8_0.1	PS- <i>b</i> -PB	45k- <i>b</i> -44k	PS	4.8k	0.1	0.47
SBD89/S4.8_0.2	PS- <i>b</i> -PB	45k- <i>b</i> -44k	PS	4.8k	0.2	0.42
SBD89/S4.8-0.3	PS- <i>b</i> -PB	45k- <i>b</i> -44k	PS	4.8k	0.3	0.37
SBD89/S4.8-0.4	PS- <i>b</i> -PB	45k- <i>b</i> -44k	PS	4.8k	0.4	0.32
SBD89/S45-0.1	PS- <i>b</i> -PB	45k- <i>b</i> -44k	PS	45k	0.1	0.47
SBD89/S45-0.2	PS- <i>b</i> -PB	45k- <i>b</i> -44k	PS	45k	0.2	0.42
SBD89/S45-0.3	PS- <i>b</i> -PB	45k- <i>b</i> -44k	PS	45k	0.3	0.37
SBD89/S45-0.4	PS- <i>b</i> -PB	45k- <i>b</i> -44k	PS	45k	0.4	0.32

^a $\omega_{hPS} = m_{hPS}/(m_{hPS} + m_{SBD})$. ^b Density of PS and PBD is considered as 1.04 and 0.9 g/cm.

Table 3.1 Detailed information of PS-*b*-PBD/hPS binary blends.

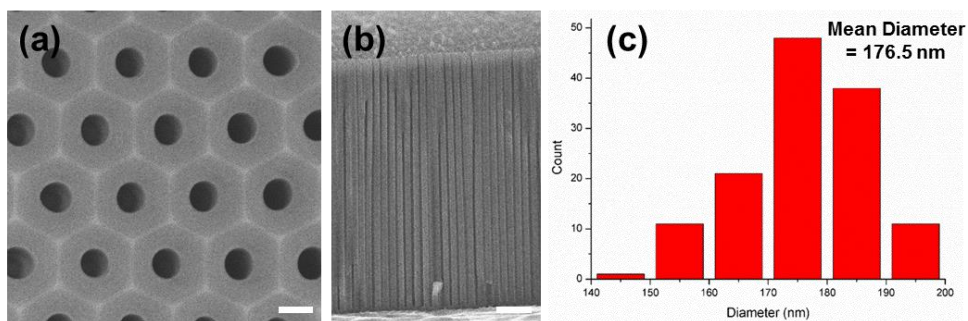


Figure 3.1. SEM images of AAO templates from (a) top view and (b) cross-sectional view. (c) Histogram representing the distribution of diameter of AAO nanopores analyzed by image analysis software (Image J). The mean diameter of pores is 176.5 ± 5.3 nm and the length is 20 μm . Scale bar is (a) 200 nm and (b) 2 μm .

3.2.2. Tunable Surface Energy Interlayer Coating to Control the Phase Behavior of Block Copolymers in 2D Confinement

Materials Diblock copolymers PS44k-*b*-PMMA45k (SMA89, Mw/Mn = 1.05) were purchased from Polymer Source, Inc., Canada. The repeat periods (L_0) of SMA89 were 42 nm. AAO templates were fabricated by the two-step anodization process.^{83,113,114} Anodization was conducted at the condition for the desired pore size: $D_p = 65$ nm (2nd Anodization in 0.3 M oxalic acid at 40V and 15 C for 1 hr, followed by 25 min of pore widening process in 10 wt % phosphoric acid solution) and $D_p = 170$ nm (same condition as 3.2.1).

Organosilicate was synthesized by the sol-gel reaction with methyl trimethoxysilane (MTMS, Aldrich) and 1,2-bis(trimethoxysilyl)ethane (BTMSE, Aldrich). The molar ratio of MTMS and BTMSE was 7:2. The acid-catalyzed hydrolysis of the mixture in THF was conducted for 30 min with HCl solution. After the hydrolysis, the mixture was condensed at 65 °C in 250 rpm of stirring for 9 hr, followed by quenching with ether. The detail synthetic procedure is described elsewhere.¹¹⁵

Preparation of OS Interlayer Coating 2.5 wt% of OS were dissolved in methyl isobutyl ketone (MIBK). AAO templates (1 × 1 cm) were dipping in OS solution for 10 min and washed by MIBK, followed by curing under vacuum at desired temperature for 6 hr. After etching out AAO templates, the structure and size of OS nanotubes were characterized.

PS-*b*-PMMA inside OS-Treated AAO Templates SMA89 were dissolved in toluene at a concentration of 2.0 wt %. 0.2 ml of polymer solution was casted onto a clean AAO template. After solvent evaporated slowly, it was completely dried in a vacuum oven and annealed under vacuum at 180 °C for 3 days. After removing

aluminum and alumina layers, free-standing polymer nanorods were dipping in 1 wt% HF aqueous solution to etch OS interlayer, followed by embedding in an epoxy resin. After curing at 60 °C for 24 hr, the epoxy-embedded samples were then cut with a diamond knife into 70 nm thin sections using a Leica Ultramicrotome.

3.3.3 Characterization

The size and shape of AAO nanopores were analyzed with a scanning electron microscope (FE-SEM, JSM- 6701F, JEOL) operated at an acceleration voltage of 10.0 kV. The morphologies of BCP and OS nanotube were characterized by a transmission electron microscope (TEM, JEM1010, JEOL) at 80.0 kV. PBD domains in SBD and PS domain in SMA were selectively stained with aqueous OsO₄ solution (2.0 wt %, Electron Microscopy Sciences) and RuO₄ solution (Electron Microscopy Science), respectively, followed by TEM characterization.

3.3. Results and Discussion

3.3.1. Microdomain Transition of Binary Blends with Low Molecular Weight hPS in 2D Confinement

The phase behavior of diblock copolymers confined in cylindrical nanochannels has extensively been studied both experimentally and by simulation^{58,116}. Both intrinsic properties of BCPs (i.e. volume fraction, interaction between consisting blocks, chain length) and interfacial factors for 2D confinement severely affect the behavior of copolymer chains, resulting in unconventional morphologies such as multiple helices, stacked disks and concentric rings. Herein, we focus more on the comparison of phase transitions of AB/A diblock copolymer/homopolymer binary blends between bulk and confined states. Also, we examined that homopolymers are solubilized in BCP microdomains in a way to facilitate BCP self-assembly under 2D confinement depending on the molecular weight of homopolymers.

In the wet-brush regime where the ratio of the chain length of hPS to that of PS block ($\alpha = M_{n,hPS}/M_{n,PS \text{ block}}$) is much lower than unity, hPS chains are allowed to be uniformly solubilized within the PS microdomains.¹¹⁷ The uniform distribution of hPS within the SBD microdomains induces the swelling of the PS domains both parallel and perpendicular to the interfaces, constraining the chain conformation of the other block (PB block). This generally leads to the phase transition of BCPs into microdomains with higher curvature to compensate the free-energy penalty caused by the conformational entropy loss of the PBD blocks. Consequently, the BCP morphology is changed from lamellae to cylinders and ultimately to spheres. Figure 3.2 shows different morphologies of self-assembled SBD42 with and without hPS4.8 confined in AAO nanopores. When $D/L_0 = 6.0$, neat SBD89 forms the morphology

of concentric rings with the outermost PB block layer (Figure 3.2a). With the low molecular weight hPS added, however, the PBD phase in microdomain changed to the helical structure due to the breaking of symmetry of the two blocks (Figure 3.2b). Although the volume fraction of PB block in the SBD42/hPS4.8 ($\omega = 20$ wt %) is 0.44, which is generally in the lamellae morphology (Table 3.1), the helical morphology was observed under cylindrical confinement. Also, we confirmed that that SBD/hPS binary blend with the same composition ($\omega = 20$ wt %) in the bulk state retains the lamellar structure. Previous works have reported that only cylinder-forming BCPs could self-assemble into helical structures under cylindrical confinement. This reflects that 2D confinement could easily invoke the symmetry breaking of BCPs upon the addition of low molecular weight homopolymers.

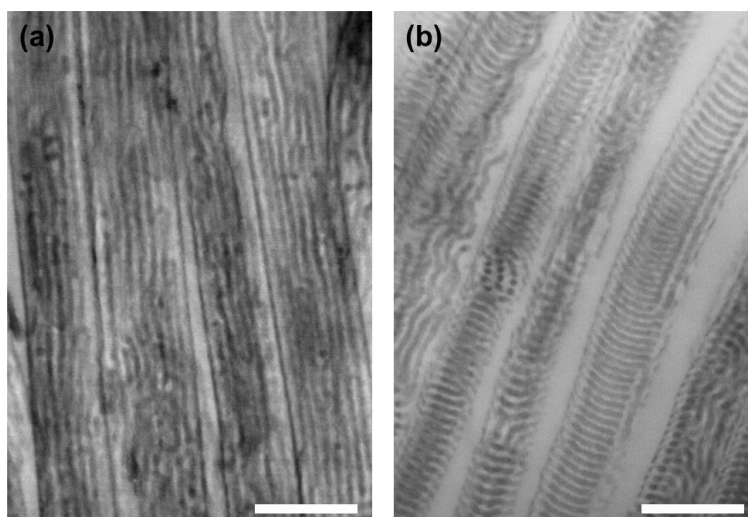


Figure 3.2. TEM images of (a) neat SBD42 and (b) binary blends with 20 wt % hPS4.8. All of the samples are stained with OsO₄ vapor before TEM investigation. Scale bar is 200 nm.

3.3.2. Comparison of the Effect of hPS Weight Fraction on the Phase Transitions in the Bulk and Confined States

To demonstrate the drastic phase transition under confinement, we investigated both bulk and confined states of SBD89/hPS4.8 ($\alpha = 0.1$) with the weight fractions of hPS4.8 varying from 0 to 40 wt % (Figure 3.3). Here, we used SBD89 instead of SBD42 to further increase the degree of confinement of the system (D/L_0 was varied from 6.0 to 4.2). In the bulk state, the lamellar structure of neat SBD89 changed to the cylindrical structure when 40 wt % hPS4.8 is added ($f_{PB} = 0.32$) (Figure 3.3a). In contrast, rapid microdomain transition occurred in the confined geometry when compared with the bulk state. The increase in the weight fraction of hPS4.8 to 20 wt % changed the PBD microdomains from concentric rings (lamellar) to helices (cylindrical) with the outermost PBD layer. Upon further increase of hPS4.8 to 30 wt % ($f_{PB} = 0.37$), spherical structure of PBD domain was finally attained (Figure 3.3b). Such strong influence of hPS addition originates from the severe constraint of copolymer chains under 2D confinement. Since hard confinement of AAO nanopores naturally make cylindrical shape of BCP assemblies, symmetric SBD forming concentric ring morphology under cylindrical confinement intrinsically had curved interface. Under this circumstance, less amount of hPS4.8 easily lead to structural transformation to peapod array (spherical) which is not obtained in bulk state with same composition. At $\omega = 30$ and 40 wt % of hPS4.8 additions, the zigzag patterns of spherical PBD domains shows the clue that a helical motif with 20 wt % hPS4.8 in the blends still exist. As the weight fraction of hPS is increased, the helical domains break up to develop spherical domains having higher curvature.

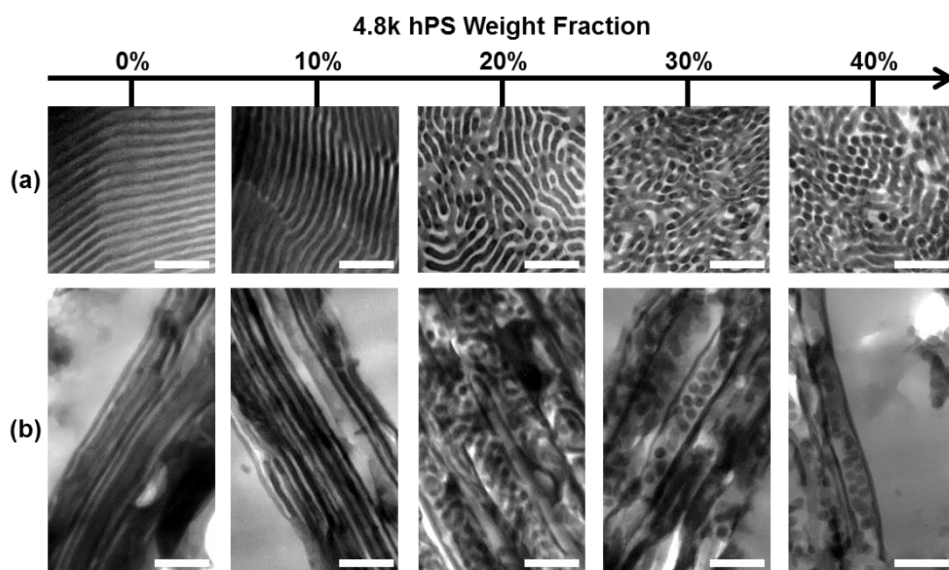


Figure 3.3. TEM images of the morphology of SBD89/hPS4.5 binary blends in (a) bulk and (b) confined state by varying the weight fraction of hPS4.5. All of the samples are stained with OsO₄ vapor before TEM investigation. Scale bar is 200 nm.

3.3.3. Effect of $M_{n,hPS}/M_{n,PS}$ Block on the Phase Transitions in Bulk and Confined States

The molecular weight of homopolymer (hPS) added to BCPs also has significant influence on the phase transition of SBD/hPS binary blends in 2D confinement. To demonstrate the effect of molecular weight of hPS, we introduced higher molecular weight homopolymer (hPS45) into BCP (SBD89) ($\alpha = 1.0$) confined in AAO nanopores with the same condition ($D/L_0 = 4.2$) (Figure 3.4). In the dry-brush regime ($\alpha \approx 1.0$), since hPS chains are locally segregated in the middle of PS block domains, the conformations of PS and PBD block chains are not obtained significantly affected by hPS as explained in the wet-brush regime.¹¹⁸ Localized hPS tends to cause the expansion of the PS microdomains followed by the eventual formation of microemulsions. In the bulk state, it is confirmed that the BCP microdomains retained lamellar morphologies with extended PS domains up to $\omega = 40$ wt % (Figure 3.4a). In the 2D confinement, on the other hand, the PS domains were swollen radially up to $\omega = 20$ wt % but microemulsion structure is eventually when w is higher than 20 wt % (Figure 3.4b). The formation of such microemulsions is believed to originate from the fragmentation of inner PBD domains. As shown in Figure 3.5, the phase transition of SBD/hPS45 under the cylindrical confinement is described. With the increase in the weight fraction of hPS45, the PBD domains were broken into droplets, forming vesicular peapod arrays (Figure 3.4b, $\omega = 40$ wt % and Figure 3.5a). Due to the hard confinement of nanochannels, not all the hPS45 could not be accommodated in the PS domains radially and the inner PBD domains were continuously pinched off to take excess hPS chains along the pore length. In contrast to the low molecular weight homopolymers, hPS45 could not be uniformly

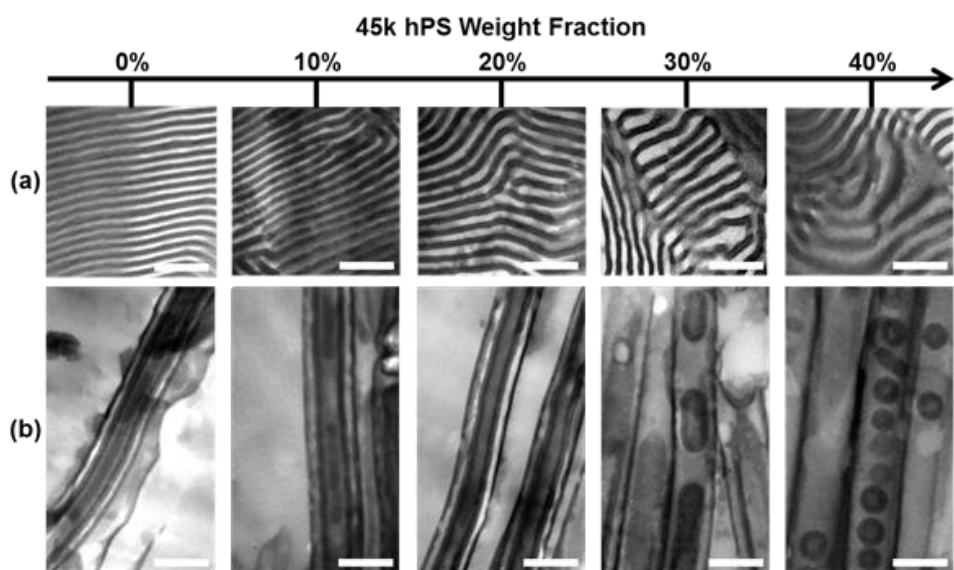


Figure 3.4. TEM images of the morphology of SBD89/hPS45 binary blends in (a) bulk and (b) confined state by varying the weight fraction of hPS45. All of the samples are stained with OsO_4 vapor before TEM investigation. Scale bar is 200 nm.

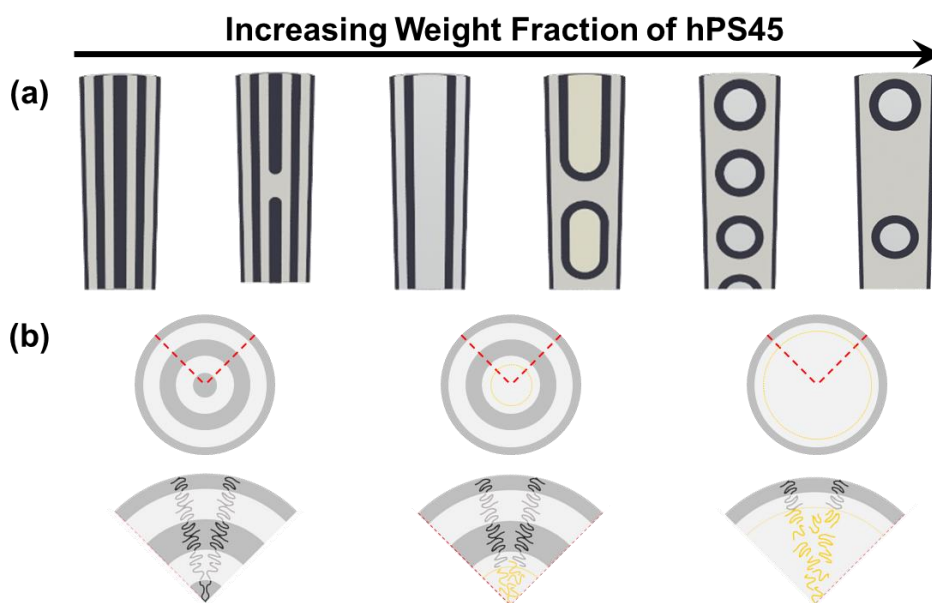


Figure 3.5. Schematic illustration of the phase transition of SBD45/hPS45 binary blends under cylindrical confinement. (a) is the view along the pore axis and (b) is the view normal to the pore diameter. As the weight fraction of hPS45 increases, hPS is preferentially located at the center of the pore. When the weight fraction of hPS45 is further increasing, the PBD layer continuous in the pore axis is broken into droplets in order to take excess hPS chains.

solubilized within the PS block and the phase transition into microemulsions of BCPs occurred. Although different molecular weight gave rise to different routes of phase transition, the transition caused by the addition of hPS under 2D confinement is more sensitive than the bulk cases.

Figure 3.6 shows that hPS45 is mainly located at the center of the nanochannels in the confined assembly of SBD89/hPS45 blends. We believe that PS microdomains were not evenly swollen along the radial direction. When $\omega = 20$ wt % of hPS45, the thickness of outer PS microdomain is retained (A in the inset of Figure 3.6a,b) while inner PS domain is swollen (B in the inset of Figure 3.6a,b). As the weight fraction of hPS45 increases up to 40 wt %, PS domain is fully expanded radially and the PBD middle layer disappeared concomitantly; the innermost PBD layer disappeared at $\omega = 20$ wt % (Figure 3.6b,e) and the next middle PBD layer eliminated at 40 wt % (Figure 3.6c,f). Since the effect of curvature is most pronounced at the center of the channels, non-ideal packing of copolymer chains is maximized in the innermost region of microdomains. Figure 3.5b shows that hPS is localized at the core as the weight fraction of homopolymer increases. To compensate for the loss of free energy induced by the large curvature at the core, hPS fill up the core region where highly stretched copolymer chains otherwise occupy (Figure 3.5b). Previous work has reported that the redistribution of homopolymers facilitated the defect-free assembly under the circumstance where the domain dimension deviates from the dimension in the bulk. Stoykovich et al. demonstrated that the local concentration of homopolymers is the highest at the sharply bent geometry to minimize the free energy of BCP assembly. Similarly, in the cylindrical confinement, excessive hPS45 are preferentially located at the center of the SBD/hPS microdomains and reduce the structural frustration imposed by the curvature.

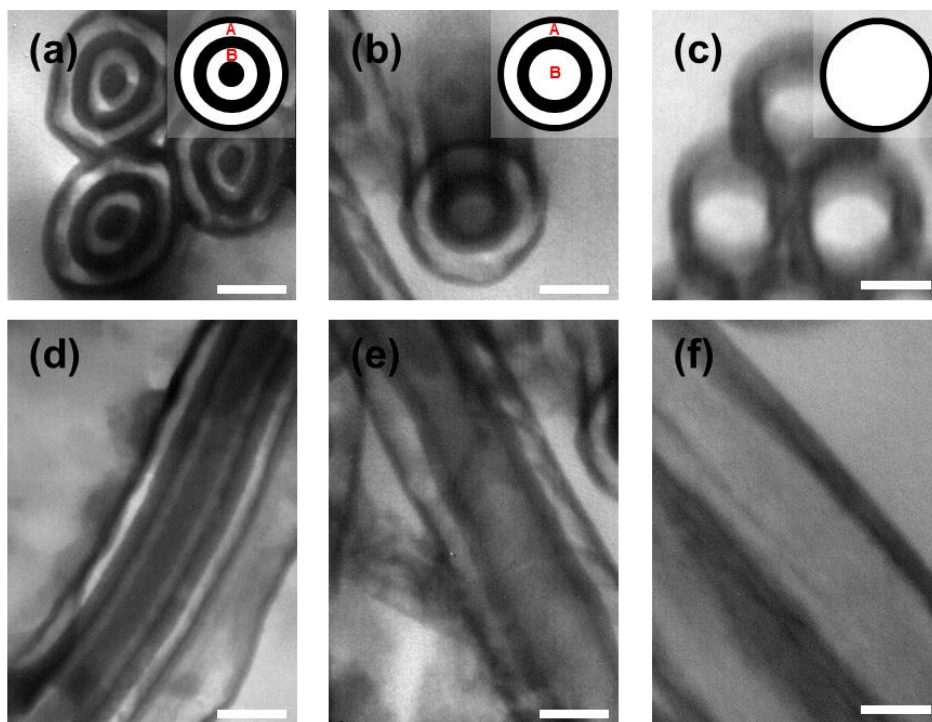


Figure 3.6. TEM images of SBD89/hPS45 confined in cylindrical pores with different fraction of hPS45 (a,d) 0, (b,e) 20, and (c,f) 40 wt %. (a) – (c) are the views normal to the pore diameter and (d) – (f) are the views along the pore axis. All the samples were stained with OsO₄ vapor before TEM investigation. Scale bars are 100 nm.

Hierarchical internal structure of self-assembled BCPs can be readily tailored with the addition of homopolymers. Tunable structures of polymer particles serve as ideal scaffolds or templates, leading to potential applications including drug delivery, catalytic supports, and optical-sensing. Polymer nanorods with various internal morphologies is obtained depending on the molecular weight of hPS. Particularly, even with the same weight fraction of hPS ($\omega = 40$ wt %), the addition of hPS4.8 changed the concentric PBD microdomains to peapod domains while vesicular morphologies where PS domains are located inside the PBD shells were obtained with the addition of hPS45 (Figure 3.7). Although the volume fraction of the PBD block in the two blends is identical, different solubilization behavior with the addition of hPS of different molecular weight leads to totally different morphological reshaping of PBD domains to minimize the free energy of the systems. Various reshaping of block copolymer morphologies only with the addition of homopolymers in nanoconfinement could be effectively used to fabricate desired hierarchical nanostructures.

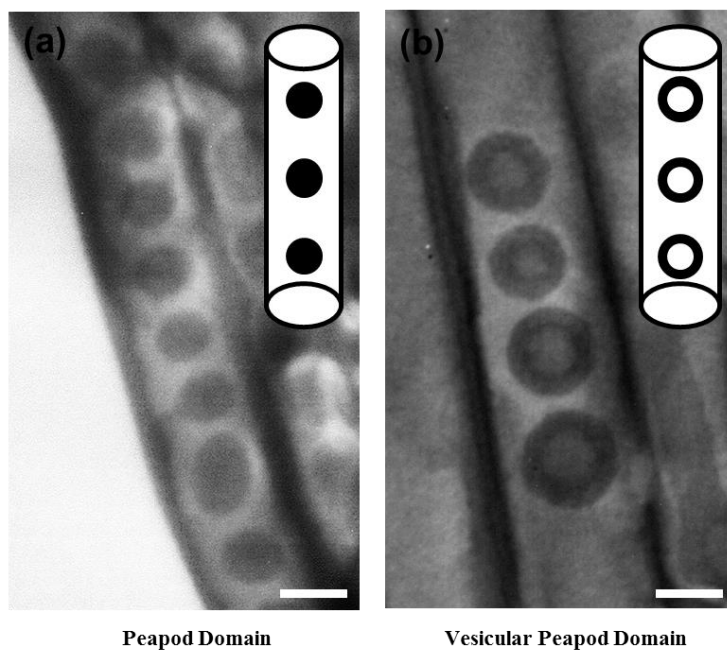


Figure 3.7. TEM images of SBD89/hPS with inverse structures upon molecular weight of hPS (a)4.8k and (b)45k hPS. (a) is normal peapod array and (b) is vesicular peapod array morphologies. All of the samples are stained with OsO₄ vapor before TEM investigation. Scale bar is 200 nm.

3.3.4. Tunable Surface Energy of OS Coating to Control the Orientation of Block Copolymers.

OS was synthesized by acid-catalyzed hydrolytic condensation of MTMS and BTMSE mixture. Prepared OS have initially a considerable amount of hydroxyl group (silanol group) owing to hydrolytic reaction. Since the silanol groups could be cross-linked into Si-O-Si bond by thermal curing, the chemical structure of OS can be controlled. As curing temperature and time increased, the ratio Si-O-Si bond to silanol group also increased. This makes it possible to control the surface energy of OS upon curing temperature. Specifically, the surface property is changed from hydrophilic to hydrophobic as the silanol groups are converted to Si-O-Si bonds. To estimate the surface energy of OS, the interfacial energy was calculated by contact angle measurement of two-liquid harmonic method and young's equation using water and diiodomethane as test liquid shown in equation 1 and 2.¹¹⁹ The contact angles of liquids on OS film which is cured at temperature ranging from 240 °C to 320 °C. (Table 3.2)

$$\gamma_{\text{liq-OS}} = \gamma_{\text{liq}} + \gamma_{\text{OS}} - \frac{4\gamma_{\text{liq}}^d \gamma_{\text{OS}}^d}{\gamma_{\text{liq}}^d + \gamma_{\text{OS}}^d} - \frac{4\gamma_{\text{liq}}^p \gamma_{\text{OS}}^p}{\gamma_{\text{liq}}^p + \gamma_{\text{OS}}^p} \quad (1)$$

$$\gamma_{\text{OS}} = \gamma_{\text{liq-OS}} + \gamma_{\text{liq}} \cos \theta_{\text{liq}} \quad (2)$$

The decrease of the total surface energy of OS upon the increase of cure temperature is affected by the changes in the relative ratio between polar and dispersive functional groups. Since silanol groups, polar fractions, are vanished by 3.8a) To control the orientation of PS-b-PMMA block copolymers, we also estimate the interfacial energy of PS and PMMA block on the OS substrate using the harmonic the condensation reaction through thermal treatment, whereas Si-CH₃ groups,

Curing Temperature (°C)	Contact Angle (°)		Surface Energy (mJ/m ²)		
	Water	CH ₂ I ₂	Dispersive	Polar	Total
240	81.8	55.9	27.51	10.95	38.46
260	86.9	59.0	26.32	8.99	35.30
280	89.6	57.4	27.23	7.62	34.86
300	91.2	58.7	26.73	7.09	33.82
320	92.0	60.5	25.93	6.95	32.89

^a The surface tension of water and diiodomethane is considered $19.9 + 52.2 = 72.1$ and $47.4 + 2.6 = 50$ mJ/m² (dispersive + polar = total surface tension), respectively.

Table 3.2. Contact angles of water and diiodomethane on OS substrates and surface energy divided by dispersive and polar fraction of OS cured at different temperature.

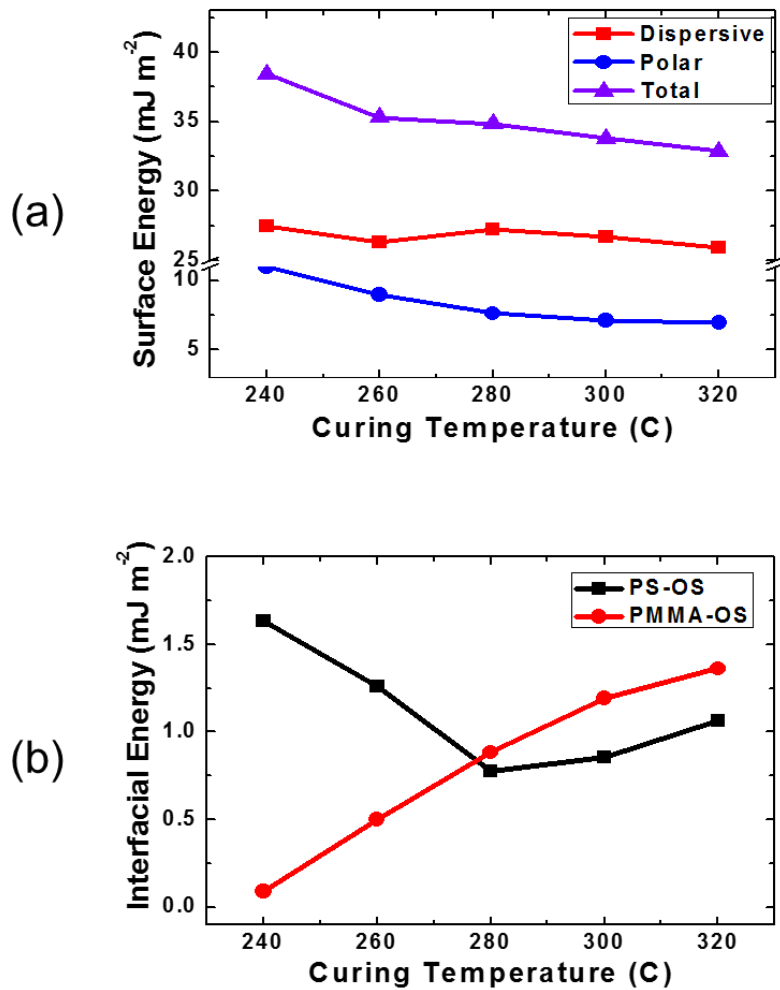


Figure 3.8. (a) Surface Energy (dispersive + polar = total) of OS as a function of curing temperature. (b) Estimated interfacial energy of PS and PMMA block on OS substrates which are cure in different temperature

dispersive fractions, are thermally stable and does not significantly change. (Figure mean equation. The surface energy of PS and PMMA are considered with reference of polymer handbook.¹²⁰ Figure 3.8b shows the surface energy of PS and PMMA block on OS substrate as a function of curing temperature. It is found that $\gamma_{\text{PMMA-OS}}$ and $\gamma_{\text{PS-OS}}$ are almost identical at curing temperature of 280 °C. At this temperature, PS and PMMA have neutral wetting orientation. We demonstrated it with SMA89 film spin-coated on pre-cured OS substrates. BCP thin film ($\sim 2.2L_0$) was annealed at 180 °C for 3days, and their morphologies are characterized by atomic force microscopy. (Figure 3.9)

we expect that the orientation of SMA89 thin film on OS substrates is determined by the interfacial energies between each block and OS, which is estimated in figure 3.8b. The OS substrate cured at 260 °C has PMMA-wetting orientation because $\gamma_{\text{PMMA-OS}}$ is much lower than that of PS-OS. Thus, a microdomain orientation parallel to the OS substrate was made (PMMA blocks are preferentially wet on the bottom OS interface, whereas PS blocks cover the free surface due to lower free surface energy than PMMA). In this asymmetric wetting, BCP thin film have commensurable condition at film thickness $\sim (n + 1/2)L_0$, where n is the integer number. Since tested film have a thickness of $2.2L_0$, hole or island structure at the free surface of films is expected as confirmed in Figure 3.9a,f, On the other hand, neutral wetting of block against the OS substrate was observed at 280 to 320 °C where the interfacial energy of each block and OS become comparable. Without any preference, the perpendicular orientation of BCP microdomains which looks fingerprint pattern was identified (figure 3.9b-d and g-i). When curing temperature was 340 °C, the interfacial energy between PS and OS substrate are lower than that of PMMA (Figure 3.8b) and PS block was wetting on both top and bottom of the

film. This is the symmetric wetting which is commensurable when the thickness of film $\sim nL_0$. As asymmetric wetting case, SMA89 had holes or islands at the free surface (Figure 3.9e,j).

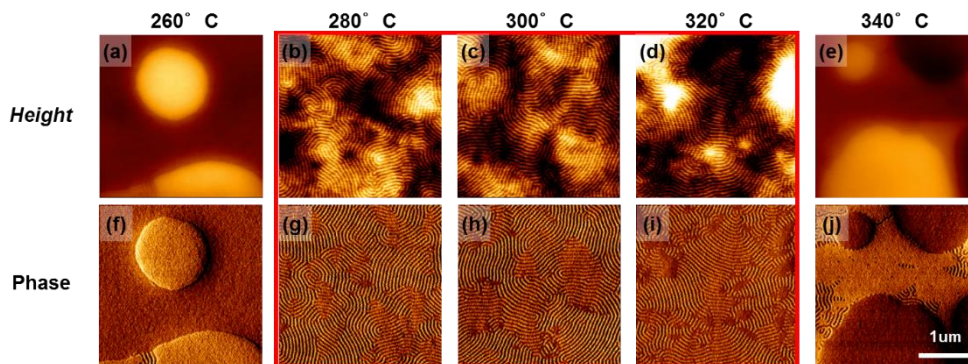


Figure 3.9. AFM height and phase images of SMA89 film annealed at 180 °C for 3 day in vacuum. BCP thin film was casted on the OS substrates pre-cured at different temperature.

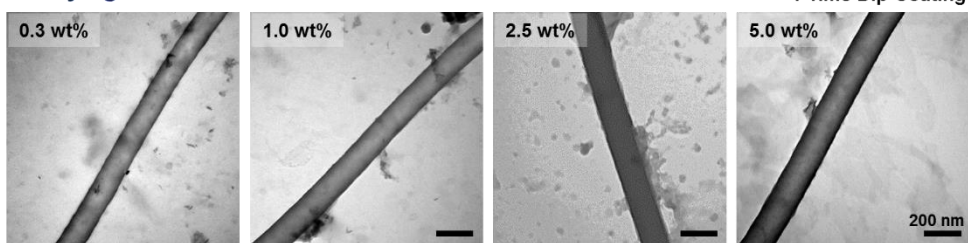
3.3.5. OS Interlayer Coating on AAO templates to Control the Orientation of Block Copolymers within Cylindrical Nano-Channels

OS interlayer was prepared by template-wetting method. Pre-made AAO template was dip-coated in OS solution for 10 min and washed in MIBK. The thickness of OS interlayer was 5 - 10 nm regardless of the concentration of OS solution and dipping time. (Figure 3.10) Since there was no preferential interaction between AAO wall and OS, only monolayer remained after washing the templates in MIBK. The regularity of interlayer coating should be confirmed because the degree of confinement is one of the most important factor to determine the phase behavior of block copolymers.

SMA89 was poured into nanochannels of AAO templates where surface is modified by OS and cured at different temperature (Figure 3.11). Bulk SMA89 formed fingerprint microdomain (lamellae) (Figure 3.11a) which made concentric ring morphology with commensurability within 2D confinement. Since D/L_0 is ~ 4 , concentric ring was observed in pristine AAO (Figure 3.11b). However, within nanochannels which were modified by OS, the orientation of microdomain was changed. In 300 °C of curing temperature for OS, the stacked lamellae were observed, meaning that the surface had neutral wetting behavior to blocks (Figure 3.11c) Even though the result is obtained with smaller diameter of nanochannels, the changes of surface property could be identified. Figure 3.11d shows the concentric lamellae with the outermost PS layer. When the OS was cured in 340 °C, the hydroxyl group was linked and the dispersive part of surface energy was dominant. It made the interfacial energy between OS and PS lower than that of PMMA. As indicated by red arrow, thin OS interlayer could be identified, which is wetted by PS block (dark region). From surface treatment, we could control the orientation of block copolymers under

2D confinement and this would be helpful in optical application since the spacing can be realized in z-axis.

• Varying Concentration of OS Solution



• Varying Dip-Coating Times

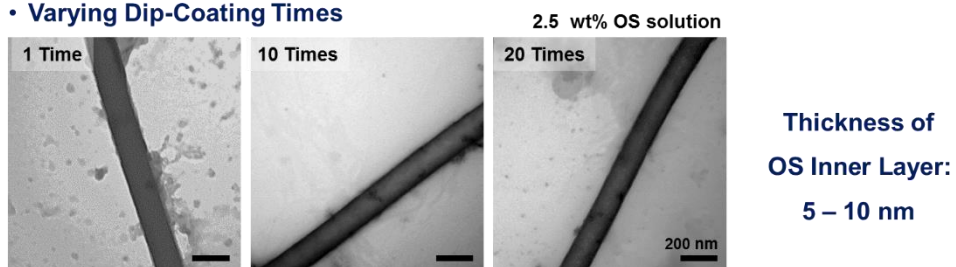


Figure 3.10. The thickness of OS interlayer coated by template wetting method characterized by TEM. The thickness is 5 - 10 nm regardless of the concentration of OS solution and dip-coating times.

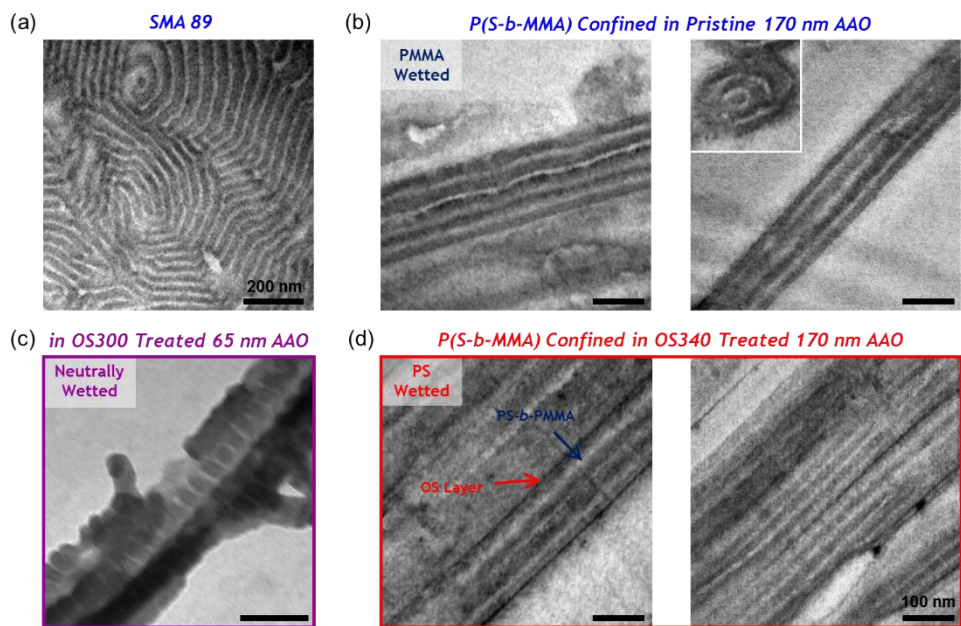


Figure 3.11. TEM images of SMA89 under (a) bulk state and confined in (b) pristine cylindrical channel of AAO and OS treated AAO at (c) 300 °C and (d) 340 °C.

3.4. Conclusion

The phase transition behavior of the BCP/homopolymer (SBD/hPS) binary blends in 2D confinement was studied in detail. The comparison of SBD/hPS blends in both bulk and confined states revealed that the constraints induced by the hard confinement significantly enhance the effect of hPS addition on the phase transition of BCPs. The addition of hPS led to the morphological transformation to compensate the loss of conformational entropy of polymer chains under 2D confinement. Depending on the molecular weight of hPS added, in particular, the phase transition of SBD/hPS blends was quite different from the bulk behavior. Low molecular weight hPS induced the structural transformation in a way to have more curved interfaces while the addition of high molecular weight hPS selectively expanded the microdomains of SBD from the center of the radial axis. Although the phase transition of SBD/hPS binary blends under confinement is significantly governed by the solubilization behavior of homopolymer chains, the phase transition in both wet- and dry-brush regimes is realized in a way to release the constraint of copolymer chains under confining geometry. The results shown here give us fundamental information on the effect of homopolymer on the phase behavior of BCP under 2D confinement to design hierarchical nanostructures of polymer particles, nanorods and vesicles. As a result, this kind of fundamental study could be effectively applied to shape the morphology of polymeric particles for versatile potential applications such as photonic crystals, optical sensors, and other fields.

Chapter 4. Self-Assembled Morphologies of Block Copolymers Confined in Conical Nanopores

4.1. Introduction

Block copolymers (BCPs) consisting of two distinctive polymer chains can self-organize into ordered nanoscale structures. Their self-assembled morphologies depend primarily on the volume ratio of the constituent blocks, chain length, and interaction between the segments.¹²¹⁻¹²⁵ To further develop and control their nanostructures and optimize corresponding properties, a variety of methods such as solvent annealing^{39,126}, additives^{127,128}, surface treatment^{31,129}, and confinement^{13,130,131} have been introduced. Especially, the nano-confinement where a spatial limitation is imposed on the chain conformation of polymers, has received much attention due to the possibility to achieve novel structures with potential applications such as lithography^{132,133}, photonic crystals¹³⁴, plasmonics¹³⁵, filtration¹³⁶, photovoltaic devices¹³⁷⁻¹³⁹, and so on. Various types of confinement using thin films, porous membranes, and emulsion droplets have been investigated both experimentally^{13,130,131,140-146} and computationally^{59,63,116,147-149}. It has been demonstrated that under confined states, besides the intrinsic properties of polymers, external factors including size, shape, surface properties, and dimensionality of the external confining environment were also crucial to the phase-separated morphologies.

For the self-assembly of BCPs under confinement, the confining environment plays an important role to determine both shape and internal morphologies of

polymeric entities. Additionally, in the case of templates with ordered patterns, hierarchical patterns of BCP microdomains could be obtained, which have potential applications such as photonics and optical materials¹⁵⁰⁻¹⁵³. For example, previous studies developed hierarchically ordered concentric silver nanoring arrays for highly sensitive surface-enhanced Raman scattering (SERS) substrates using BCP confined in ordered cavities. Even though hierarchically ordered nanopatterns in two-dimension have been studied, the development of fabrication routes for hierarchical 3D nanostructures with controllable nanosized domains still remains a challenge.

In the present work, we report a strategy to control the morphologies of poly(styrene-*b*-1,4 butadiene) (PS-*b*-PB) confined within conical nanopores. While previous work studied the self-assembly of chained molecules under confinement using symmetric environment such as cylinders and spheres, the phase-behavior of block copolymers within asymmetric geometries has rarely been addressed so far. With both experimental and theoretical analyses of the geometric effects of conical nanopores, we systematically investigate the competitive interplay of thermodynamic parameters on the self-assembly of block copolymers within asymmetric geometry. The size, shape, and surface properties of the nanopores were controlled in order to investigate enthalpic and entropic factors on the self-assembly of BCPs. The loss of conformational entropy induced by the large curvature at the vertices was the critical parameter to determine the orientation of BCP microdomains within such asymmetric pores. Specifically, while stacked lamellae perpendicular to the depth were observed for small-sized conical pores, concentric lamellae replicating the geometry of confining matrix were obtained in large cones and cylindrical pores. As the size and shape of the pores were varied, intermediate morphologies were also obtained. Computational results based on the simulated

annealing method with parameters matched to experiment was also calculated to compare observed morphologies. Calculated results relating to the interfacial energies between blocks, the entropic penalty induced by chain stretching, and the surface energy between blocks and pore wall were quantitatively described in order to elucidate how the interplay between thermodynamic factors contributed to the equilibrium morphologies.

Since nanoscale pattern of BCP have a possibility to be hybridized with the metal nanoparticles, a periodic array of metallic domains on a nanoscale can be utilized in optical applications. Additionally, in our research, BCP matrix conforms to the surface topology of nanopores and conical geometry are known to induce the strong electronic and magnetic enhancement at the vertices.¹⁵³⁻¹⁵⁷ The synergetic effect of the shape and periodic pattern of BCPs could play a significant role as effective electromagnetic properties. These works pave the way for the potential platform of optical metamaterials, leading to a variety of applications.

4.2. Experimental

Materials A high purity aluminum foil (99.999 %) with 0.5 mm thickness were purchased from Good Fellow, UK and used after degreased in acetone and isopropanol solution. Diblock Copolymers PS_{20k}-*b*-PB_{22k} (SBL42, $f_{PB} = 0.55$, $M_w/M_n = 1.03$) and 4k hydroxyl end-functionalized PS (PS-OH, $M_w/M_n = 1.03$) was purchased from Polymer Source, Inc., Canada. The repeat period (L_0) of SBL42 were 30 nm. Epoxy resin consisting of Embed 812, dodecenylsuccin anhydride (DDSA), nadic methyl anhydride (NMA) and DMP-30 was purchased from Ted Pella and used after mixing the components as manual. 70 % Perchloric acid, oxalic acid, 85 % phosphoric acid, ethanol, toluene was purchased from Sigma-Aldrich and used as received.

Fabrication of AAO Templates Various size and shape of nanopores were prepared as confining templates. The experimental procedure to fabricate the nanopores are described in Chapter 2. The detailed information of prepared nanopores including the diameter (D_p), the radius of curvature at the bottom (r_c), and aspect ratio ($AR = h/D_p$).

Modifying Surface Properties of Inner Wall of Conical Pores Surface-modified AR3 conical pores were prepared by anchoring monohydroxyl-terminated PS (PS-OH) onto pre-made AAO templates.^{158,159} 2.5 wt % PS-OH solution dissolved in toluene was spin-cast on AAO templates, followed by annealing at 180 °C under vacuum to graft PS chains onto AAO inner walls. The reaction time was varied to control the grafting density of PS chains and unreacted PS-OH chains were removed by repeated washing and sonication in toluene.

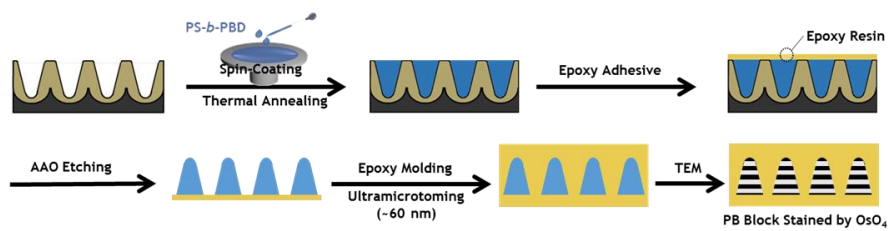


Figure 4.1. Schematics for experimental procedure for characterizing morphologies of PS-*b*-PB.

Types of pore	Diameter (D_p)	Radius of curvature at the bottom (r_c)	Aspect ratio ($AR = h/D_p$)
Small conical pores	80 nm	15 nm	2, 3, 5
Large conical pores	240 nm	80 nm	2, 3, 5
Small truncated conical pores	80 nm	40 nm	2, 3, 5
Small cylindrical pores	80 nm	80 nm	2, 3, 5

Table 4.1. List of various types of pore and their diameter (D_p), radius of curvature at the bottom (r_c), and aspect ratio ($AR = h/D_p$).

PS-*b*-PBD within AAO Templates To fill various types of pores completely, 1.5 to 5.0 wt % of PS-*b*-PB solution dissolved in toluene were spin-cast and spin rate was controlled from 1500 to 3000 rpm. After dried in a vacuum oven for 24 hr, the samples were annealed under vacuum at 125 °C for 4 days. To prevent the release of polymer nanocones during removing AAO templates, the samples were fixed using epoxy adhesive and cured at 60 °C for 12 hr. The aluminum layer was chemically etched using copper chloride (3.0 wt %) / hydrochloric acid (50 wt %) aqueous mixture and alumina was removed by sodium hydroxide aqueous solution (5.0 wt %), followed by embedded in epoxy resin and cured at 60 °C for 48 hr. Embedded samples were then sectioned with a diamond knife using a Leica Ultramicrotome.

Characterization The top and cross-sectional view of nanopores were identified using a scanning electron microscope (FE-SEM, JSM-6701F, JEOL Ltd.) operated at an acceleration voltage of 10.0 kV. The morphologies of PS-*b*-PB were analyzed with a transmission electron microscope (TEM, JEM1010, JEOL Ltd.) at 80.0 kV. 2.0 wt % aqueous solutions of OsO₄ were used to stain PB block selectively.

For morphological observations in 3D using TEMT, the PS-*b*-PB within AAO template was ultramicrotomed to a thickness of 100 nm by using an ultramicrotome (UC7, Leica microsystems, Germany) with a diamond knife at – 80 °C. We note here that we made thin section without chemical etching. The ultrathin section was transferred onto a Cu mesh with elastic carbon film as a supporting membrane. The thin section was stained with OsO₄ vapor (1,000 Pa) for 1 hr.

Prior to the electron microscopy experiments; gold nanoparticles (diameter: 5 nm) were placed on the backside of supporting membrane. The thin section was observed by a TEM operated at 200 kV (JEM-2200FS, JEOL Ltd.), and the system was equipped with a slow-scan CCD camera (Gatan USC 4000, Gatan Inc.). A series

of TEM images were acquired at the tilt angles of $\pm 70^\circ$ in 1° step. The TEM images were aligned by the fiducial marker method¹⁶⁰ with Au nanoparticles deposited on a supporting membrane. After the alignment, the tilt series of the TEM images were reconstructed by a filtered back projection algorithm.

Simulation Method The simulations were conducted using a simulated annealing method on a lattice model. Previous studies had established the validity of the method for studying the self-assembly of block copolymers under the confined state. The model and algorithm for the calculation are concisely described below, whereas detailed information can be found elsewhere³³⁻³⁵. Model diblock copolymers of A_7B_5 were used in the study, and the volume fraction of A blocks is given by $f_A = 0.58$, which form lamellae in the bulk. The model chains are confined to a conical pore embed in a cubic lattice with a total segment concentration of $\rho = 0.85$. The bond length, connecting two consequent segments on a chain is set to 1 and $\sqrt{2}$ lattice spacing, and therefore each site has 18 nearest neighbor sites. In the model system, only interactions due to the nearest-neighbor sites are considered. In all cases, the repulsion between a pair of A-B segment is modeled by an interaction parameter $\epsilon_{AB} = 1.0k_B T_{ref}$, where k_B is the Boltzmann constant and T_{ref} is a reference temperature. Interactions between the air surface (U) and chain segments are set to $-\epsilon_{AU} = \epsilon_{BU} = \epsilon_{AB} = 1.0$. The surface-polymer interactions, $\epsilon_{A\omega}$ and $\epsilon_{B\omega}$, have the form of $-\epsilon_{A\omega} = \epsilon_{B\omega} = \alpha\epsilon_{AB}$ and α is varied from 0 to 1. Other interactions are set to be zero. The annealing schedule with $T_j = fT_{j-1}$ is applied, where T_j is the temperature in the j th annealing step and f is a scaling factor with a value the same as that used earlier³⁵. The annealing temperature of $T_1 = 100T_{ref}$, and the final temperature is fixed at $T_F = 1.4T_{ref}$ for convenient comparison.

4.3. Results and Discussion

4.3.1. Self-Assembled Morphologies of Block Copolymer within Conical Nanopores

We prepared nanopores with various shape and size by two-step anodization and the fabrication method are described in Chapter 2 and Figure 4.1. Detailed information for the nanopores including the diameter (D_p), depth (h), aspect ratio ($AR = h/D_p$), and the radius of curvature at the bottom (r_c) was listed in Table 4.1. Lamella-forming BCPs, PS_{20k}-*b*-PB_{22k} (SBL42, $f_{PB} = 0.55$) with a repeat period (L_0) of 30 nm were used in this study. To systematically investigate the effects of various factors on the phase-separation of PS-*b*-PB under conical confinement, controlled studies with different pore sizes, surface properties, and bottom geometries were carried out (Figure 4.2).

Figure 4.3 presents SEM images of cross-sectional and top (inset) view of small and large conical pores. Although tapered pores were produced using the stepwise process of anodization and pore widening, the inner surface of pores was smooth owing to the multiple times of short reaction and the roughness of the inner wall did not influence the self-assembly of copolymer chain. The diameters of each pore were 80 and 240 nm and the depths were controlled to have an aspect ratio of 2,3 and 5.

Besides different D_p , they had different radii of curvature at the bottom and their bottom diameters (D_B) were 15 and 80 nm. Since the ratio between D_B and L_0 was less than unity, the large curvature of small conical pores could induce much severe entropic penalty on the chain conformation of copolymers than that of large pores.

In order to completely fill the conical pores with SBL42 using spin-coating, the concentration of polymer solution and spin-rate were varied. After thermal annealing

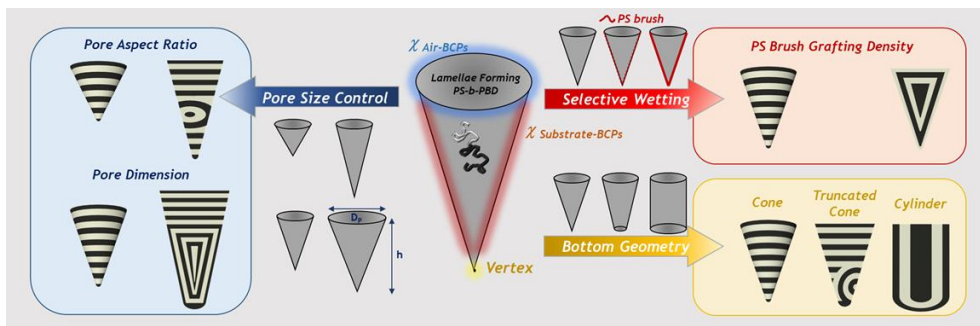


Figure 4.2. Schematic illustration of the self-assembled morphologies of lamellae-forming PS-*b*-PB under conical nano-confinement.

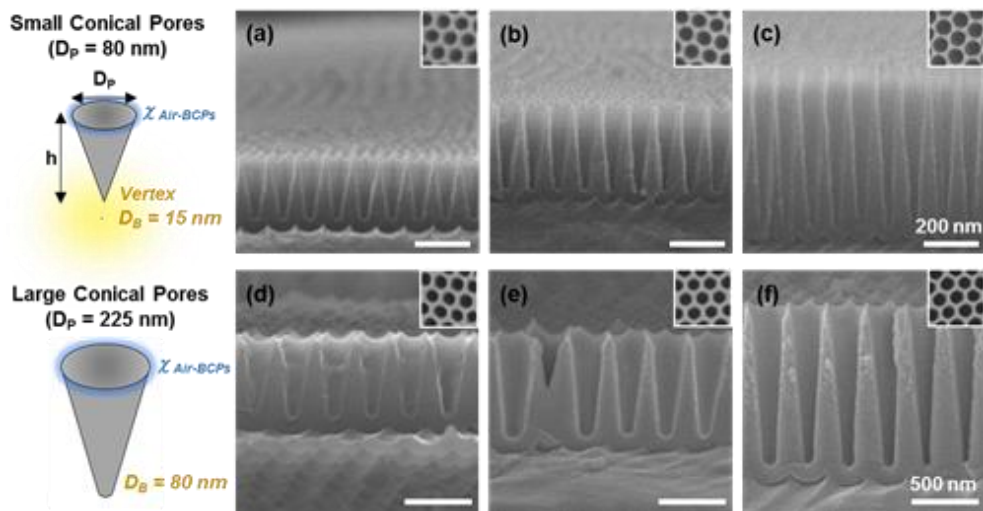


Figure 4.3. SEM Images of cross-sectional view of conical pores. Small and large conical pores have 80 nm (a-c) and 225 nm (d-f) of pore diameter (D_p). Both size of pores were fabricated to have various aspect ratio ($AR = h/D_p$, h is a depth of pore); 2 (a,d), 3 (b,e) and 5 (c,f). Inset of the images are top-view of corresponding pores.

under vacuum for 4 days, epoxy resin was cast on the sample to prevent the release of polymer nanocones and the AAO templates were then removed by the etchant solution. The internal morphologies of the BCP nanocones were investigated by transmission electron microscopy (TEM). OsO₄ was used to selectively stain the PB blocks and prevent damage during the epoxy embedding process.

TEM images (Figure 4.4) show completely different orientation of SBL42 microdomains confined within small and large conical pores. Although previous works demonstrated preferential wetting of PB blocks to AAO walls^{94,95}, stacked lamellae perpendicular to the pore depth (stacked lamellae) was obtained within AR2 and AR3 small conical pores (Figure 4.4a,b). This morphology was expected for the small conical pores due to severe confinement at the vertices. Since the radius of curvature was much smaller than L_0 of SBL42, the loss of conformational entropy near the bottom was too large to make energetically favored orientation. Additionally, PB blocks were located at the air surface due to lower surface free energy, and this orientation propagated to the bottom which also contributed to stacked lamellar structures. Even though these effects from the bottom and top of the pores were also microdomain (Figure 4.4c). As pore depth increased, the influence of the top and bottom surfaces was diminished and block copolymer chains were assembled in a way to have a lower interfacial energy between polymer blocks and AAO surfaces. Since the characteristic lengths of small conical pores (h , D_p , and r_c) were comparable to L_0 of SBL42, the self-assembly within small conical pores was identified in AR5 small cones, mixed orientation was observed in the middle of predominantly affected by the confinement rather than other energetic factors.

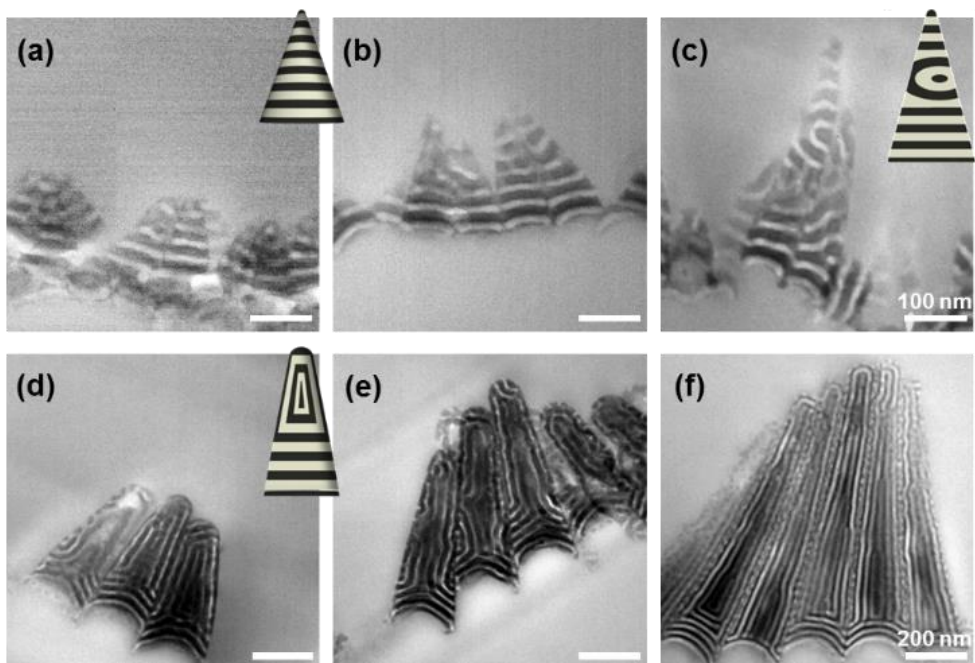


Figure 4.4. TEM Images of the morphology of SBL42 nanocones confined in various size of conical pores; small and large BCP nanocones with diameter of 80 nm (a-c) and 225 nm (d-f). Both small and large nanocones have three aspect ratio (h/D_p); 2 (a,d), 3 (b,e) and 5 (c,f). All of the samples were stained with OsO_4 vapor before TEM investigation and PB block appear dark in images.

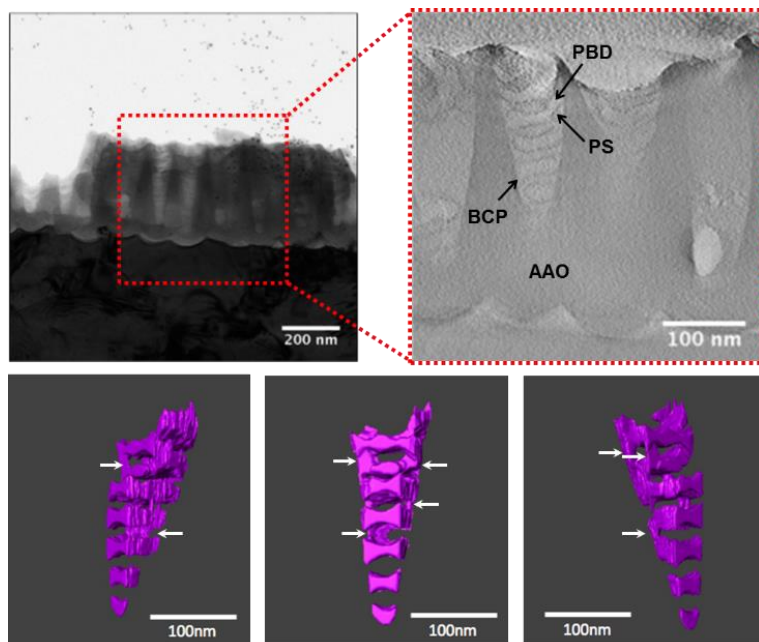


Figure 4.5. 3D imaging of SBL42 confined in AR3 small conical pores using TEM tomography. AAO templates is not removed. A digitally sliced electron tomography image shows the cross section of AAO templates containing BCPs parallel to the pore axis. Here, only OsO₄ stained PB microdomains (dark region) are extracted in purple color. White arrows in magnified view indicate partially connected PB domain at the interface between polymers and pore surfaces.

In contrast to the case of small cones, lamellae parallel to the cone surface (concentric lamellae) with the outermost PB layers were mostly observed in larger nanocones, even though stacked lamellae caused by the surface energy still appeared near the pore entrance (Figure 4.4d-f). Since the degree of confinement in large pores was much lower than that in small pores, the interaction between polymers and substrates mainly influence the phase-separation of BCPs. Overall, the morphologies of BCP nanocones were determined in order to minimize the free energy of the system associated with the effect of wall selectivity and confinement.

Since the ordered nanostructure of BCPs can be hybridized with metal nanoparticle for other application, it is important to analyze the surface topology in detail. Annealed BCP samples within AAO templates was directly visualized using cryo-microtoming and transmission electron microtomography (TEMT)¹⁶⁰ in order to gain more detailed information on their three-dimensional structures and the internal morphologies of BCP nanocones (Figure 4.5). The sample where block copolymers remained within AR3 conical pores was directly microtomed at $-80\text{ }^{\circ}\text{C}$ by a diamond knife, followed by staining with OsO_4 . In figure 4.5, only PB microdomains were extracted from 3D electron tomography and visualized as purple color. As indicated by the white arrows, structural analysis with TEMT revealed that PB domains were partially connected at the interface between polymers and pore surfaces. Even though BCP microdomains had the perpendicular orientation to the pore surfaces, pore surfaces were still weakly selective to PB blocks, and therefore the segregation of PB chains was favorable in terms of surface energy of the wall (E_s). This interfacial undulation was also confirmed from the simulation data, as discussed later section.

4.3.2. Effect of Bottom Geometry on Chain Conformation of Block Copolymers

To gain deeper insight for the entropic loss induced by the curvature at the bottom, additional pores with different bottom geometries, i.e. truncated conical pores with the same D_p and aspect ratio as conical pores and cylindrical pores, were introduced (Figure 4.6). To make truncated conical pores, pre-made conical pores with $D_p = 60$ nm were chemically etched to widen the pore radially. As etching time increased, the radius of curvature at the bottom also increased and there was more space to accommodate the BCP chains. Cylindrical pores were fabricated by conventional two-step anodization and fully widened to make 80 nm of pore diameters. Since r_c of each pore was 40 and 80 nm, respectively, which were larger than L_0 of SBL42, different phase-behavior of SBL42 from conical pores was expected.

Figure 4.7 shows the morphologies of SBL42 confined within AAO templates as functions of pore shape and aspect ratio. TEM images of BCP nanocones which were inserted in Figure 4.4 were reiterated for the comparison and categorization with the morphologies of others. For all types of shapes, the morphologies of SBL42 changed with aspect ratio. For AR2 truncated cones, stacked lamellae were observed due to the free surface energy of air surface as nanocones (Figure 4.7d). However, in the case of AR3 and AR5, mixed orientation where stacked lamellae and surface wetted orientation coexisted started to appear (Figure 4.7e,f). Since the entropic penalty of polymer chains at the bottom decreased, the effect of interfacial energy between blocks and AAO wall became dominant and contributed to the morphological transition of BCP microdomains. In the AR2 cylinder, stacked lamellae with undulated orientation at the bottom were observed (Figure 4.7g). It

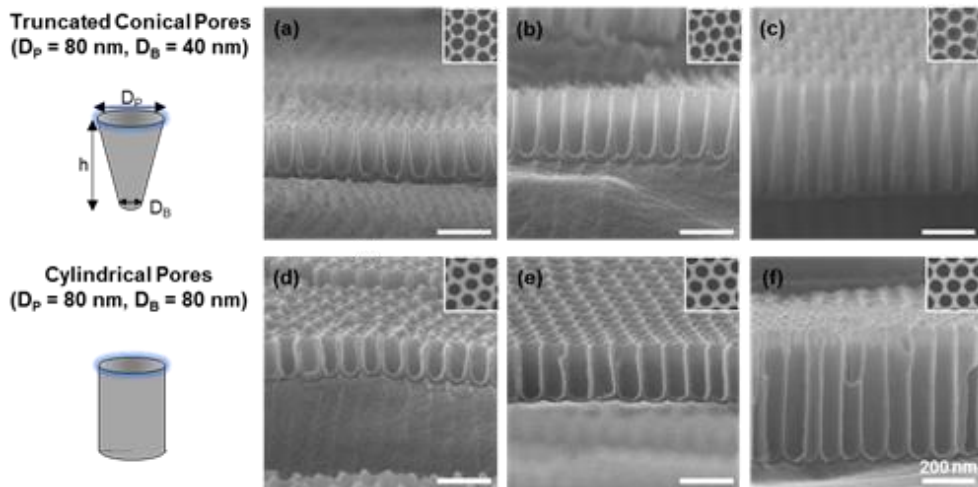


Figure 4.6. SEM Images of cross-sectional view of AAO pores with different bottom shapes; small (a-c) truncated conical and (d-f) cylindrical pores. All types of pore have 80 nm of top diameter and bottom diameters were controlled to have 40 and 80 nm, respectively, which are larger than 15 nm of conical pore. All pores were fabricated to have three aspect ratio (h/D_p); 2 (a,d), 3 (b,e) and 5 (c,f). Inset of all the images are top-view of corresponding pores.

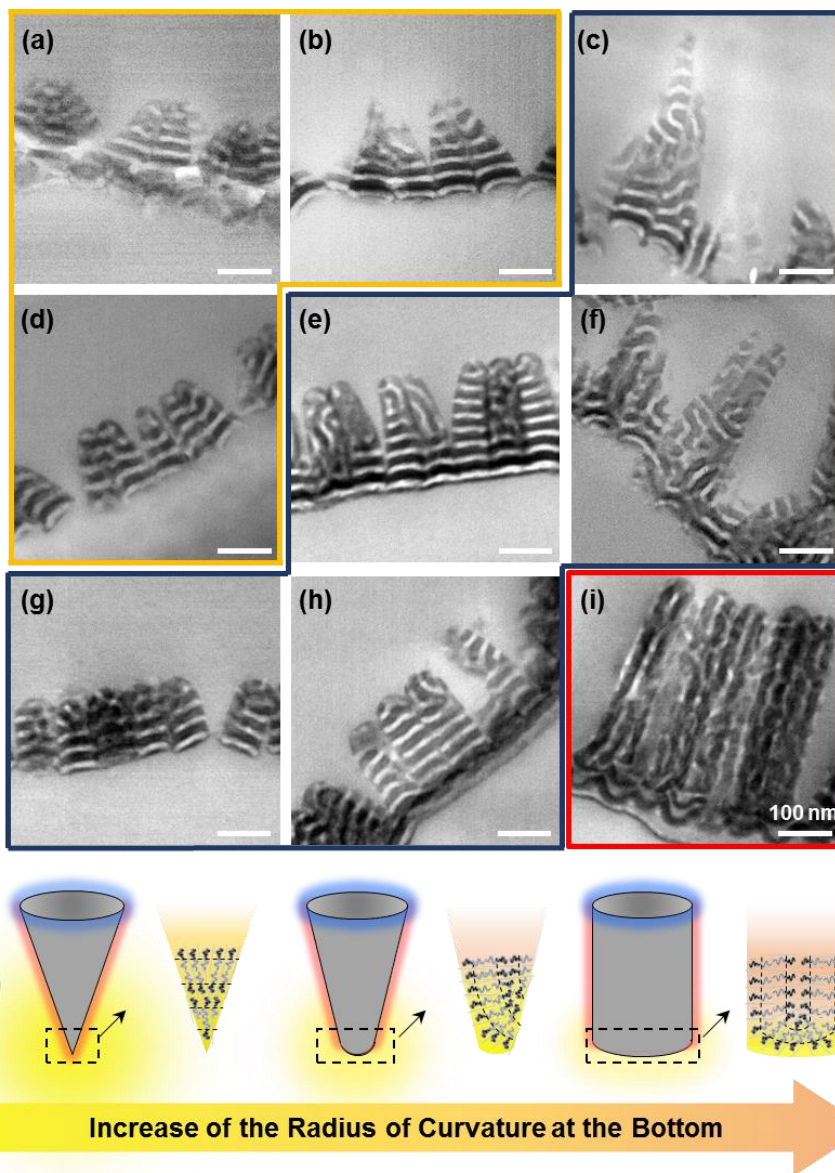


Figure 4.7. TEM Images of the morphology of SBL42 confined within small (a-c) conical, (d-f) truncated conical, and (g-i) cylindrical pores. All of the samples were stained with OsO_4 vapor before TEM investigation. The images in yellow, blue and red box correspond to groups of stacked lamellae, mixed orientation, and concentric lamellae, respectively. (j) The schematic of comparative thermodynamic parameters and corresponding microdomain orientation depending on different shapes of the pore bottom.

showed that increase of bottom diameter gave more space to accommodate the copolymer chains, thus inducing the observed morphological transition. Previous works also revealed that high curvature of the bottom and neutral selectivity of the wall led to interfacial undulation as seen in Fig 4.7g.¹⁵⁸ As the depth of pore increased, mixed orientation appears in AR3 (Figure 4.7h) and concentric lamellae were apparently observed in AR5 cylinder (Figure 4.7i).

Overall, the morphologies of BCPs were categorized into three groups: stacked lamellae, mixed orientation, and concentric lamellae (yellow, blue and red box in Figure 4.7). The self-assembled morphologies of SBL42 could be explained by the competitive interplay between thermodynamic parameters: the free surface energy of the blocks, the interfacial energy between blocks and AAO walls, and the entropic penalty due to the curvature at the vertices as illustrated in Figure 4.7j. As the pore shapes changed from cone to truncated cone to cylinder, the curvatures at the vertices were decreasing and there was a less entropic penalty on chain conformation. Also, as pore depth increased, the influences from the top and bottom of the pores were diminished. Therefore, the surface preference played a significant role in phase-separation of BCPs and surface-wetted orientation of BCP chains was preferred.

4.3.3. Changes in Wetting Behavior of Block Copolymer Confined within Conical Nanopores

To demonstrate the effect of interfacial energy, the surface property of substrates was modified by hydroxyl-terminated PS (PS-OH) brushes. PS-OH solutions were spin-coated on AR3 conical pores and annealed under vacuum to graft PS brushes onto the inner wall of pores. To control the surface energy, the annealing time was varied from 20 min to 120 hr, which was related to the grafting density of PS chains.¹⁵⁸ After washing out unreacted polymer chains, SBL42 was filled in pores and the morphologies were characterized by TEM observation (Figure 4.8). In 20 min of annealing, PS and PB domains looked entangled, indicating that the selectivity of wall surfaces was changed (Figure 4.8a). As annealing time increased, selective wetting orientation with the outermost PS layer started to appear in the middle of the pore domain (Figure 4.8b). This orientation propagated to vertices and sequentially bottom of BCP nanocones and concentric lamellar structures eventually observed in 120 hr annealed samples (Figure 4.8c,d). We speculated that the increased selectivity of substrate walls overwhelmed the entropic effect of vertices and sequentially energetic effect of air surface, meaning the energetic effect from air surface is the most influential parameter on the self-assembled morphologies under conical confinement.

To compare the experimental and simulative data for the phase-transition upon the surface property of walls, the simulation work for the lamellar morphologies confined in AR3 conical pores as a function of the surface-polymer interaction, $\epsilon_{A\omega}$ was also conducted using simulated annealing method presented in Figure 4.8e. The volume ratio of BCPs and the relative size of pores were chosen to match the

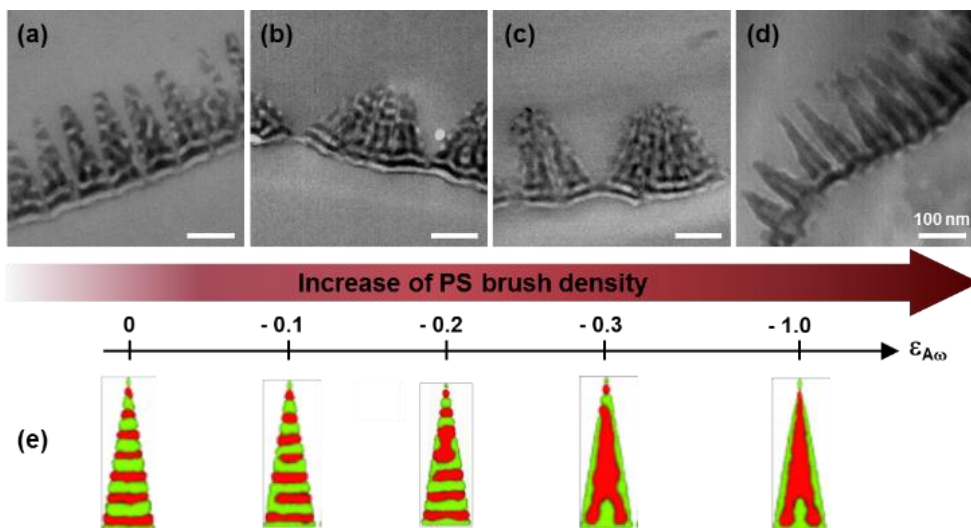


Figure 4.8. TEM Images of the morphology of SBL42 confined in AR3 small conical pores modified by PS-OH brush. The grafting density of PS brushes were controlled by reaction time: (a) 20 min, (b) 1, (c) 48, and (d) 120 hr. All of the samples were stained with OsO_4 vapor before TEM investigation. (e) Simulated morphologies of block copolymers as a function of interfacial energy between A blocks and confining walls ($\epsilon_{A\omega}$).

experimental parameters. The surface preferences were characterized by the wall - A block interaction, $\varepsilon_{A\omega} = -\varepsilon_{B\omega}$. Polymer chains in green and red color in the snapshot correspond to A and B blocks, respectively. Other specifications including simulation parameters and procedure were described in detail in the Experimental Section. Stacked lamellae observed in the limit of $\varepsilon_{A\omega} \approx 0$ changed to mixed orientation in the middle of microdomain at -0.2 of $\varepsilon_{A\omega}$. From $\varepsilon_{A\omega} = -0.3$, surface wetted orientation propagated to air surface and eventually to vertices when the selectivity of the wall was maximized ($\varepsilon_{A\omega} = -1.0$). It is interesting to note that the order of transition to the surface wetted orientation was different from experimental results in that the entropic loss at the vertices was much influential than the enthalpic effect of air surface. This difference was caused by imperfect match of simulation parameters such as the curvature at the vertices and free surface energy of constituent blocks. Nevertheless, both experimental and simulative results implied that the phase separation of block copolymers under conical confinement was comparatively affected by confinement-induced entropy loss of polymer chains and the interfacial energies with surroundings.

4.3.4. Effect of Molecular Weight of Block Copolymers

Figure 4.9 shows the self-assembled morphologies of SBL26 ($L_0 = 22$ nm) confined within small conical pores. While AR2 SBL26 made stacked lamellae (figure 4.9a), both stacked lamellae and concentric lamellae was observed in AR3 and AR5 SBL26 nanocones (figure 4.9b,c). Since the ratio between bottom diameter to repeat period (D_B/L_0) of SBL26 was 0.73, larger than 0.5 in SBL42 small cones, the constraint from the pore tip was much less and there was more freedom of chain conformation to make energetically favorable assembly. This result indicated that sharp vertices effectively confined the copolymer chains and governed the self-assembly of block copolymers. The degenerated structures in AR3 and AR5 could be induced by the size of nanopores which were not perfectly regular.

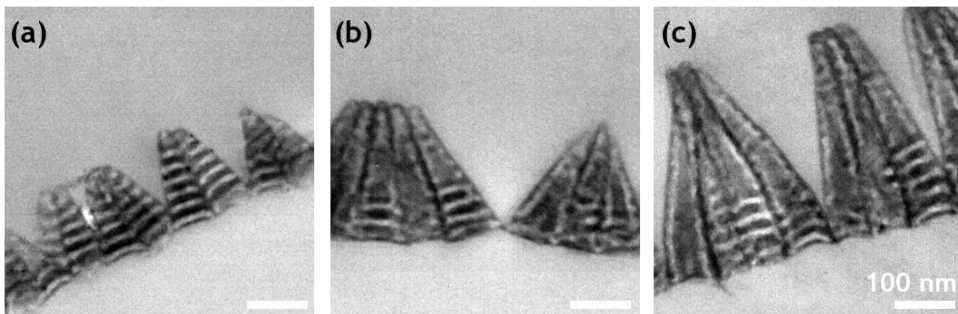


Figure 4.9. TEM images of the morphology of SBL26 confined in small conical pores. BCP nanocones have diameter of 80 nm and various aspect ratio (h/D_p); (a) AR 2, (b) AR 3 and (c) AR 5. All of the samples were stained with OsO_4 vapor before TEM investigation.

4.3.5. Enthalpic and Entropic Contribution in the Free Energy of Block Copolymers within Conical Confinement

A series of simulations as functions of pore sizes, pore shapes, and surface preference was performed to investigate the effects of the competitive parameters thoroughly (Figure 4.10 and Figure 4.11). Based on the simulation data in Fig 4.8e, we concluded that the surface was weakly selective to PB block in our experiments, which was consistent with previous studies by Russel's group.⁹⁴ Therefore, calculated morphologies for weak selectivity ($\epsilon_{A\omega} = -0.2$) in Figure 4.10 showed a good agreement with experimental observation in Figure 4.4 and 4.7. Other simulated morphologies with controlled interaction parameters were also described. Three competitive parameters affecting the phase-separation of BCPs were estimated in the following way: (1) the A-B interfacial energy (E_i), (2) the surface energy (E_s), and (3) the entropic cost ΔS of stretching chains. (Figure 4.11) Two energetic components ($E = E_s + E_i$) were computed, and the third component (entropy) was estimated in a mean-field sense by the mean-square end-to-end distance of chains. As deduced early³³⁻³⁵, constraining ends of a chain to have a separation R leads to a conformational entropy reduction of $\Delta S = -3R^2/2Nb^2$, and a free energy increase of $\Delta F = 3TR^2/2Nb^2$ per chain, where b is the segment length. The total free energy F was calculated as a function of surface interaction: $F = E_i + E_s + \Delta F^*N_C$, where N_C is the number of chains in the system. With a comparison of the plot and morphologies in each case, it was noted that when the surfaces were strongly preferential to the A block ($\epsilon_{A\omega} \leq -0.3$), F was dominated by E_s , and therefore concentric structures with outermost A layer were observed. In this case, lower surface energy compensated entropic loss induced by chain stretching. For neutral

wetting case ($\varepsilon_{A\omega} = \varepsilon_{B\omega} = 0$), F was dominated by E_i , the same as that in the bulk case, and flat lamellar structures were formed regardless of aspect ratio and pore shapes. At intermediate wettability between the two limiting cases, it was also the competition between the enthalpic and entropic free energies that determined the phase-separated structure of a system. For the case of cylindrical confinement, E_s was lower than that for conical or truncated conical confinement cases due to larger surface area, which resulted in the formation of concentric cylinder (AR5) and mixed orientation (AR2 and 3) at even weak preferential wetting value ($\varepsilon_{A\omega} = -0.1 - 0.2$). When mixed orientation was formed, polymer chains were highly stretched whereas the interfacial energy became lower.

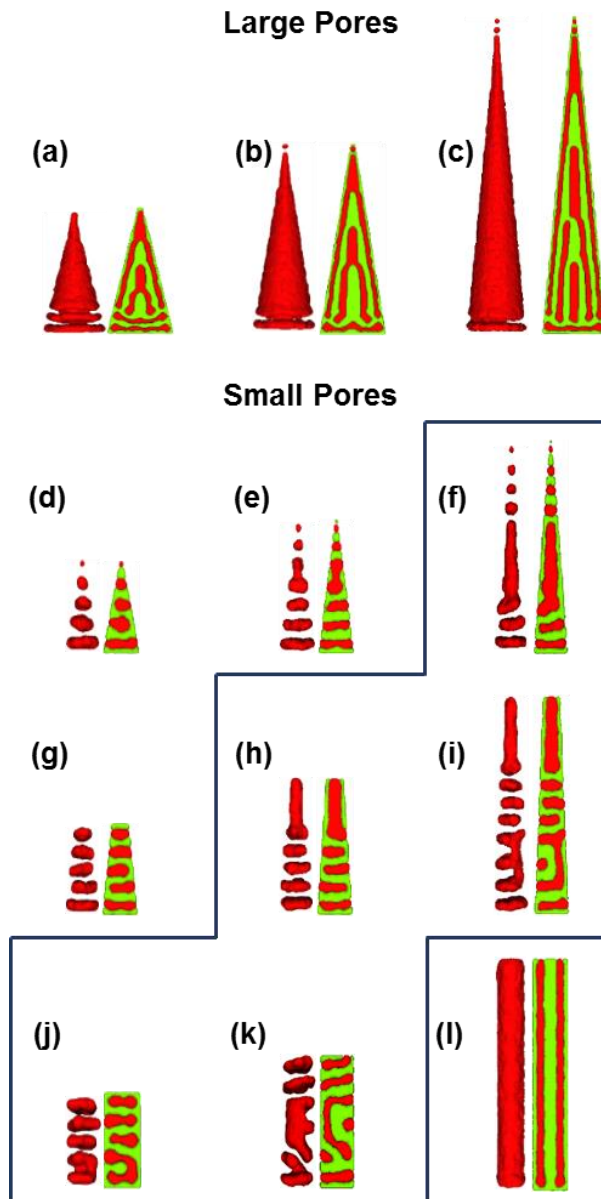


Figure 4.10. Simulated morphologies of block copolymers A_7B_5 as functions of sizes and shapes of confining pores; (a-c) large conical pores with D_p/L_0 of 7.37 and (d-f) small conical, (g-i) truncated conical, (j-l) cylindrical pores with D_p/L_0 of 2.53. Both small and large BCP pores have three aspect ratio; 2 (a,d,g,j), 3 (b,e,h,k) and 5 (c,f,i,l). The interaction of surface is fixed at $\epsilon_{A\omega} = -0.2$ and $\epsilon_{B\omega} = 0.2$

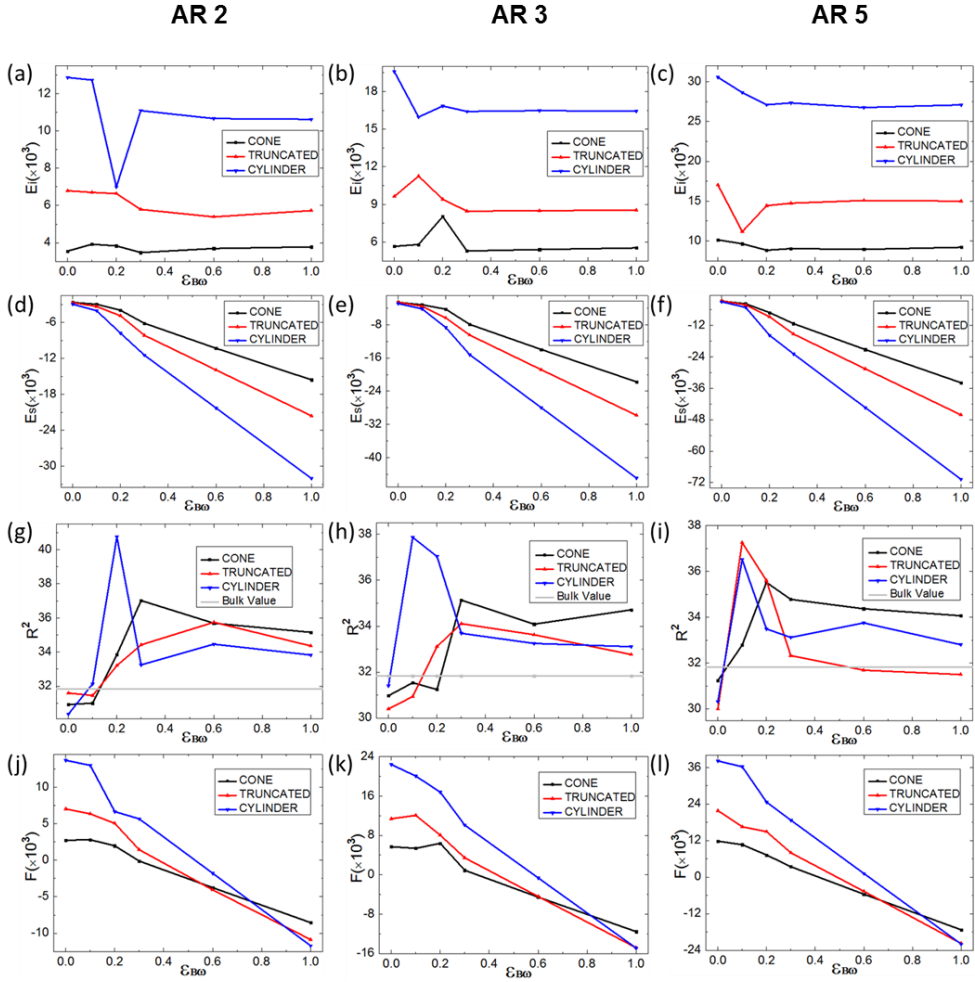


Figure 4.11. (a-c) The A-B interfacial energy (E_i), (d-f) the surface energy (E_s), (g-i) the mean-square end-to-end distance of chains, and (j-l) the total free energy of block copolymers A_7B_5 as a function of ϵ_{B0} . The ratio between pore diameter and repeat period (D_p/L_0) is 2.53.

4.4. Conclusion

We systematically investigated the self-assembled morphologies of PS-*b*-PB confined in conical pores with various pore sizes, shapes and surface properties. The controllable environment for the confinement allowed consistent observation of the BCP morphologies and their dependence on the various thermodynamic factors. Increasing the radius of curvature from conical to truncated conical to cylindrical pores resulted in a morphological transition from the stacked lamellae to the concentric lamellae. As the loss of conformational entropy decreased, the interaction between pore surfaces became more dominant parameter to determine the phase-separation of BCPs. The surface energy of pore wall was also varied to elucidate the competitive interplay between the thermodynamic parameters and the order of influence was identified by both experimental and simulative results. Quantitative analysis including interfacial energies (E_i and E_s) and end-to-end distance of chains revealed how block copolymers self-assembled in order to minimize the free energy of the system. Since BCP matrix formed hierarchically patterned 3D nanostructures and conical structures had a possibility to enhance electromagnetic properties strongly, this work can be used as a platform for nanophotonic and plasmonic devices.

Bibliography

- (1) Khandpur, A. K.; Foerster, S.; Bates, F. S.; Hamley, I. W.; Ryan, A. J.; Bras, W.; Almdal, K.; Mortensen, K. *Macromolecules* **1995**, *28*, 8796-8806.
- (2) Matsen, M. W.; Bates, F. S. *Macromolecules* **1996**, *29*, 1091-1098.
- (3) Sakurai, S. *Polymer* **2008**, *49*, 2781-2796.
- (4) Koo, K.; Ahn, H.; Kim, S.-W.; Ryu, D. Y.; Russell, T. P. *Soft Matter* **2013**, *9*, 9059-9071.
- (5) Hamley, I. W. *Nanotechnology* **2003**, *14*, R39-R54.
- (6) Park, C.; Yoon, J.; Thomas, E. L. *Polymer* **2003**, *44*, 7779.
- (7) Darling, S. B. *Progress in Polymer Science* **2007**, *32*, 1152-1204.
- (8) Luo, M.; Epps, T. H. *Macromolecules* **2013**, *46*, 7567-7579.
- (9) Marencic, A. P.; Register, R. A. *Annual Review of Chemical and Biomolecular Engineering* **2010**, *1*, 277-297.
- (10) Stoykovich, M. P.; Nealey, P. F. *Materials Today* **2006**, *9*, 20-29.
- (11) Hawker, C. J.; Russell, T. P. *MRS Bulletin* **2005**, *30*, 952-966.
- (12) Segalman, R. A. *Materials Science and Engineering: R: Reports* **2005**, *48*, 191-226.
- (13) Fasolka, M. J.; Mayes, A. M. *Annual Review of Materials Research* **2001**, *31*, 323-355.
- (14) Angelescu, D. E.; Waller, J. H.; Register, R. A.; Chaikin, P. M. *Advanced Materials* **2005**, *17*, 1878-1881.
- (15) Angelescu, D. E.; Waller, J. H.; Adamson, D. H.; Deshpande, P.; Chou, S. Y.; Register, R. A.; Chaikin, P. M. *Advanced Materials* **2004**, *16*, 1736-1740.
- (16) Albalak, R. J.; Thomas, E. L. *Journal of Polymer Science Part B: Polymer Physics* **1994**, *32*, 341-350.
- (17) Chen, Z.-R.; Kornfield, J. A.; Smith, S. D.; Grothaus, J. T.; Satkowski, M. M. *Science* **1997**, *277*, 1248-1253.
- (18) Osuji, C.; Zhang, Y.; Mao, G.; Ober, C. K.; Thomas, E. L. *Macromolecules* **1999**, *32*, 7703-7706.
- (19) Park, C.; Simmons, S.; Fetters, L. J.; Hsiao, B.; Yeh, F.; Thomas, E. L.

- Polymer* **2000**, *41*, 2971-2977.
- (20) Mansky, P.; DeRouchey, J.; Russell, T. P.; Mays, J.; Pitsikalis, M.; Morkved, T.; Jaeger, H. *Macromolecules* **1998**, *31*, 4399-4401.
- (21) Liedel, C.; Pester, C. W.; Ruppel, M.; Lewin, C.; Pavan, M. J.; Urban, V. S.; Shenhar, R.; Bösecke, P.; Böker, A. *ACS Macro Letters* **2013**, *2*, 53-58.
- (22) Ruppel, M.; Pester, C. W.; Langner, K. M.; Sevink, G. J. A.; Schoberth, H. G.; Schmidt, K.; Urban, V. S.; Mays, J. W.; Böker, A. *ACS Nano* **2013**, *7*, 3854-3867.
- (23) Gurovich, E. *Physical Review Letters* **1995**, *74*, 482-485.
- (24) Thurn-Albrecht, T.; Schotter, J.; Kästle, G. A.; Emley, N.; Shibauchi, T.; Krusin-Elbaum, L.; Guarini, K.; Black, C. T.; Tuominen, M. T.; Russell, T. *Science* **2000**, *290*, 2126-2129.
- (25) Tao, Y.; Zohar, H.; Olsen, B. D.; Segalman, R. A. *Nano Letters* **2007**, *7*, 2742-2746.
- (26) Majewski, P. W.; Gopinadhan, M.; Jang, W.-S.; Lutkenhaus, J. L.; Osuji, C. O. *Journal of the American Chemical Society* **2010**, *132*, 17516-17522.
- (27) Majewski, P. W.; Osuji, C. O. *Langmuir* **2010**, *26*, 8737-8742.
- (28) Majewski, P. W.; Gopinadhan, M.; Osuji, C. O. *Journal of Polymer Science Part B: Polymer Physics* **2012**, *50*, 2-8.
- (29) Son, J. G.; Bulliard, X.; Kang, H.; Nealey, P. F.; Char, K. *Advanced Materials* **2008**, *20*, 3643-3648.
- (30) Ji, S.; Liu, C.-C.; Son, J. G.; Gotrik, K.; Craig, G. S. W.; Gopalan, P.; Himpsel, F. J.; Char, K.; Nealey, P. F. *Macromolecules* **2008**, *41*, 9098-9103.
- (31) Suh, H. S.; Kang, H.; Liu, C.-C.; Nealey, P. F.; Char, K. *Macromolecules* **2010**, *43*, 461-466.
- (32) Gu, W.; Hong, S. W.; Russell, T. P. *ACS Nano* **2012**, *6*, 10250-10257.
- (33) Bang, J.; Bae, J.; Löwenhielm, P.; Spiessberger, C.; Given-Beck, S. A.; Russell, T. P.; Hawker, C. J. *Advanced Materials* **2007**, *19*, 4552-4557.
- (34) Ryu, D. Y.; Shin, K.; Drockenmuller, E.; Hawker, C. J.; Russell, T. P. *Science* **2005**, *308*, 236-239.
- (35) Albert, J. N. L.; Young, W.-S.; Lewis, R. L.; Bogart, T. D.; Smith, J. R.; Epps, T. H. *ACS Nano* **2012**, *6*, 459-466.
- (36) Jung, Y. S.; Ross, C. A. *Advanced Materials* **2009**, *21*, 2540-2545.

- (37) Xuan, Y.; Peng, J.; Cui, L.; Wang, H.; Li, B.; Han, Y. *Macromolecules* **2004**, *37*, 7301-7307.
- (38) Zhang, M.; Yang, L.; Yurt, S.; Misner, M. J.; Chen, J.-T.; Coughlin, E. B.; Venkataraman, D.; Russell, T. P. *Advanced Materials* **2007**, *19*, 1571-1576.
- (39) Kim, S. H.; Misner, M. J.; Xu, T.; Kimura, M.; Russell, T. P. *Advanced Materials* **2004**, *16*, 226-231.
- (40) Stoykovich, M. P.; Kang, H.; Daoulas, K. C.; Liu, G.; Liu, C.-C.; de Pablo, J. J.; Müller, M.; Nealey, P. F. *ACS Nano* **2007**, *1*, 168-175.
- (41) Segalman, R. A.; Hexemer, A.; Hayward, R. C.; Kramer, E. J. *Macromolecules* **2003**, *36*, 3272-3288.
- (42) Ouk Kim, S.; Solak, H. H.; Stoykovich, M. P.; Ferrier, N. J.; de Pablo, J. J.; Nealey, P. F. *Nature* **2003**, *424*, 411-414.
- (43) Xiao, S.; Yang, X.; Edwards, E. W.; La, Y.-H.; Nealey, P. F. *Nanotechnology* **2005**, *16*, S324-S329.
- (44) Segalman, R. A.; Yokoyama, H.; Kramer, E. J. *Advanced Materials* **2001**, *13*, 1152-1155.
- (45) Chuang, V. P.; Cheng, J. Y.; Savas, T. A.; Ross, C. A. *Nano Letters* **2006**, *6*, 2332-2337.
- (46) Jung, Y. S.; Jung, W.; Ross, C. A. *Nano Letters* **2008**, *8*, 2975-2981.
- (47) Chuang, V. P.; Gwyther, J.; Mickiewicz, R. A.; Manners, I.; Ross, C. A. *Nano Letters* **2009**, *9*, 4364-4369.
- (48) Jung, Y. S.; Chang, J. B.; Verploegen, E.; Berggren, K. K.; Ross, C. A. *Nano Letters* **2010**, *10*, 1000-1005.
- (49) Ilievski, F.; Ross, C. A. *Journal of Vacuum Science & Technology B* **2010**, *28*, 42-44.
- (50) Mishra, V.; Hur, S.-m.; Cochran, E. W.; Stein, G. E.; Fredrickson, G. H.; Kramer, E. J. *Macromolecules* **2010**, *43*, 1942-1949.
- (51) Thomas, E. L.; Kinning, D. J.; Alward, D. B.; Henke, C. S. *Macromolecules* **1987**, *20*, 2934-2939.
- (52) Stoykovich, M. P.; Müller, M.; Kim, S. O.; Solak, H. H.; Edwards, E. W.; de Pablo, J. J.; Nealey, P. F. *Science* **2005**, *308*, 1442-1446.
- (53) Yoon, B.; Huh, J.; Ito, H.; Frommer, J.; Sohn, B.-H.; Kim, J. H.; Thomas, E. L.; Park, C.; Kim, H.-C. *Advanced Materials* **2007**, *19*, 3342-3348.

- (54) Rockford, L.; Liu, Y.; Mansky, P.; Russell, T. P.; Yoon, M.; Mochrie, S. G. J. *Physical Review Letters* **1999**, *82*, 2602-2605.
- (55) Xiang, H.; Shin, K.; Kim, T.; Moon, S.; Mccarthy, T. J.; Russell, T. P. *Journal of Polymer Science Part B: Polymer Physics* **2005**, *43*, 3377-3383.
- (56) Xu, Y.; Li, W.; Qiu, F.; Yang, Y.; Shi, A.-C. *The Journal of Physical Chemistry B* **2009**, *113*, 11153-11159.
- (57) Yu, B.; Sun, P.; Chen, T.; Jin, Q.; Ding, D.; Li, B.; Shi, A.-C. *The Journal of Chemical Physics* **2007**, *126*, 204903.
- (58) Yu, B.; Jin, Q.; Ding, D.; Li, B.; Shi, A.-C. *Macromolecules* **2008**, *41*, 4042-4054.
- (59) Yu, B.; Sun, P.; Chen, T.; Jin, Q.; Ding, D.; Li, B.; Shi, A.-C. *The Journal of chemical physics* **2007**, *127*, 114906.
- (60) Ma, M.; Thomas, E. L.; Rutledge, G. C.; Yu, B.; Li, B.; Jin, Q.; Ding, D.; Shi, A.-C. *Macromolecules* **2010**, *43*, 3061-3071.
- (61) Higuchi, T.; Tajima, A.; Motoyoshi, K.; Yabu, H.; Shimomura, M. *Angewandte Chemie International Edition* **2008**, *47*, 8044-8046.
- (62) Pinna, M.; Hiltl, S.; Guo, X.; Böker, A.; Zvelindovsky, A. V. *ACS Nano* **2010**, *4*, 2845-2855.
- (63) Yu, B.; Li, B.; Jin, Q.; Ding, D.; Shi, A.-C. *Macromolecules* **2007**, *40*, 9133-9142.
- (64) Chen, P.; Liang, H.; Shi, A.-C. *Macromolecules* **2008**, *41*, 8938-8943.
- (65) Anker, J. N.; Hall, W. P.; Lyandres, O.; Shah, N. C.; Zhao, J.; Van Duyne, R. P.: Biosensing with plasmonic nanosensors. In *Nanoscience and Technology: A Collection of Reviews from Nature Journals*; World Scientific, 2010; pp 308-319.
- (66) Keddie, J. L.; Jones, R. A.; Cory, R. A. *EPL (Europhysics Letters)* **1994**, *27*, 59.
- (67) Guo, L. J. *Advanced materials* **2007**, *19*, 495-513.
- (68) Huang, Z.; Fang, H.; Zhu, J. *Advanced materials* **2007**, *19*, 744-748.
- (69) Murray, C. B.; Kagan, a. C.; Bawendi, M. *Annual review of materials science* **2000**, *30*, 545-610.
- (70) Martín, J.; Manzano, C. V.; Martín-González, M. *Microporous and Mesoporous Materials* **2012**, *151*, 311-316.

- (71) Martín, J.; Nogales, A.; Martín-González, M. *Macromolecules* **2013**, *46*, 1477-1483.
- (72) Masuda, H.; Fukuda, K. *science* **1995**, *268*, 1466-1468.
- (73) Nielsch, K.; Choi, J.; Schwirn, K.; Wehrspohn, R. B.; Gösele, U. *Nano letters* **2002**, *2*, 677-680.
- (74) Martín, J.; Vázquez, M.; Hernández-Vélez, M.; Mijangos, C. *Journal of Nanoscience and Nanotechnology* **2009**, *9*, 5898-5902.
- (75) Masuda, H.; Satoh, M. *Japanese Journal of Applied Physics* **1996**, *35*, L126.
- (76) Keller, F.; Hunter, M.; Robinson, D. *Journal of the Electrochemical Society* **1953**, *100*, 411-419.
- (77) Lee, W.; Ji, R.; Gösele, U.; Nielsch, K. *Nature materials* **2006**, *5*, 741.
- (78) Choi, M. K.; Yoon, H.; Lee, K.; Shin, K. *Langmuir* **2011**, *27*, 2132-2137.
- (79) Kelly, K. L.; Coronado, E.; Zhao, L. L.; Schatz, G. C. *The Journal of Physical Chemistry B* **2003**, *107*, 668-677.
- (80) Cho, Y.; Kim, G.; Cho, Y.; Lee, S. Y.; Minsky, H.; Turner, K. T.; Gianola, D. S.; Yang, S. *Advanced Materials* **2015**, *27*, 7788-7793.
- (81) Lee, Y.; Lee, J.; Lee, T. K.; Park, J.; Ha, M.; Kwak, S. K.; Ko, H. *ACS applied materials & interfaces* **2015**, *7*, 26421-26429.
- (82) Lee, W.; Park, S.-J. *Chemical reviews* **2014**, *114*, 7487-7556.
- (83) Li, A.; Müller, F.; Birner, A.; Nielsch, K.; Gösele, U. *Journal of applied physics* **1998**, *84*, 6023-6026.
- (84) Kanamori, Y.; Hane, K.; Sai, H.; Yugami, H. *Applied Physics Letters* **2001**, *78*, 142-143.
- (85) Boden, S. A.; Bagnall, D. M. *Applied Physics Letters* **2008**, *93*, 133108.
- (86) Lee, M. J.; Lee, N. Y.; Lim, J. R.; Kim, J. B.; Kim, M.; Baik, H. K.; Kim, Y. S. *Advanced Materials* **2006**, *18*, 3115-3119.
- (87) O'sullivan, J.; Wood, G. *Proceedings of the Royal Society of London. A. Mathematical and Physical Sciences* **1970**, *317*, 511-543.
- (88) Masuda, H.; Asoh, H.; Watanabe, M.; Nishio, K.; Nakao, M.; Tamamura, T. *Advanced Materials* **2001**, *13*, 189-192.
- (89) Chen, B.; Lu, K.; Tian, Z. *Langmuir* **2010**, *27*, 800-808.
- (90) Choi, S.-J.; Yoo, P. J.; Baek, S. J.; Kim, T. W.; Lee, H. H. *Journal of the American Chemical Society* **2004**, *126*, 7744-7745.

- (91) Cheng, J. Y.; Mayes, A. M.; Ross, C. A. *Nat Mater* **2004**, *3*, 823-828.
- (92) Mansky, P.; Russell, T. P.; Hawker, C. J.; Pitsikalis, M.; Mays, J. *Macromolecules* **1997**, *30*, 6810-6813.
- (93) Yang, X. M.; Peters, R. D.; Nealey, P. F.; Solak, H. H.; Cerrina, F. *Macromolecules* **2000**, *33*, 9575-9582.
- (94) Dobriyal, P.; Xiang, H.; Kazuyuki, M.; Chen, J.-T.; Jinnai, H.; Russell, T. P. *Macromolecules* **2009**, *42*, 9082-9088.
- (95) Shin, K.; Xiang, H.; Moon, S. I.; Kim, T.; McCarthy, T. J.; Russell, T. P. *Science* **2004**, *306*, 76-76.
- (96) Sun, Y.; Steinhart, M.; Zschech, D.; Adhikari, R.; Michler, G. H.; Gösele, U. *Macromolecular Rapid Communications* **2005**, *26*, 369-375.
- (97) Coakley, K. M.; McGehee, M. D. *Applied Physics Letters* **2003**, *83*, 3380-3382.
- (98) Kang, Y.; Walish, J. J.; Gorishnyy, T.; Thomas, E. L. *Nature Materials* **2007**, *6*, 957-960.
- (99) Park, C.; Yoon, J.; Thomas, E. L. *Polymer* **2003**, *44*, 6725-6760.
- (100) Hashimoto, T.; Tanaka, H.; Hasegawa, H. *Macromolecules* **1990**, *23*, 4378-4386.
- (101) Matsen, M. W. *Macromolecules* **1995**, *28*, 5765-5773.
- (102) Winey, K. I.; Thomas, E. L.; Fetters, L. J. *Macromolecules* **1992**, *25*, 2645-2650.
- (103) Jeon, K.-J.; Roe, R.-J. *Macromolecules;(United States)* **1994**, *27*.
- (104) Nagpal, U.; Kang, H.; Craig, G. S.; Nealey, P. F.; de Pablo, J. J. *Acs Nano* **2011**, *5*, 5673-5682.
- (105) Stoykovich, M. P.; Edwards, E. W.; Solak, H. H.; Nealey, P. F. *Physical review letters* **2006**, *97*, 147802.
- (106) Stoykovich, M. P.; Muller, M.; Kim, S. O.; Solak, H. H.; Edwards, E. W.; de Pablo, J. J.; Nealey, P. F. *Science* **2005**, *308*, 1442-1446.
- (107) Xu, J.; Yang, Y.; Wang, K.; Li, J.; Zhou, H.; Xie, X.; Zhu, J. *Langmuir* **2015**, *31*, 10975-10982.
- (108) Yang, R.; Li, B.; Shi, A.-C. *Langmuir* **2011**, *28*, 1569-1578.
- (109) Xu, J.; Wang, K.; Liang, R.; Yang, Y.; Zhou, H.; Xie, X.; Zhu, J. *Langmuir* **2015**, *31*, 12354-12361.

- (110) Mansky, P.; Liu, Y.; Huang, E.; Russell, T. P.; Hawker, C. *Science* **1997**, *275*, 1458-1460.
- (111) Son, J. G.; Kang, H.; Kim, K.-Y.; Lee, J.-S.; Nealey, P. F.; Char, K. *Macromolecules* **2011**, *45*, 150-158.
- (112) Suh, H. S.; Kang, H.; Nealey, P. F.; Char, K. *Macromolecules* **2010**, *43*, 4744-4751.
- (113) Furneaux, R.; Rigby, W.; Davidson, A. *Nature* **1989**, *337*, 147-150.
- (114) Masuda, H.; Fukuda, K. *science* **1995**, *268*, 1466.
- (115) Lee, J.-K.; Char, K.; Rhee, H.-W.; Ro, H. W.; Yoo, D. Y.; Yoon, D. Y. *Polymer* **2001**, *42*, 9085-9089.
- (116) Yu, B.; Sun, P.; Chen, T.; Jin, Q.; Ding, D.; Li, B.; Shi, A.-C. *Physical review letters* **2006**, *96*, 138306.
- (117) Tanaka, H.; Hasegawa, H.; Hashimoto, T. *Macromolecules* **1991**, *24*, 240-251.
- (118) Koizumi, S.; Hasegawa, H.; Hashimoto, T. *Macromolecules* **1994**, *27*, 6532-6540.
- (119) Wu, S. In *Tilte*1971; Wiley Online Library.
- (120) Handbook, P.; Brandrup, J.; Immergut, E.; Grulke, E.
- (121) Bates, F. S. *Science* **1991**, *251*, 898-905.
- (122) Bates, F. S.; Fredrickson, G. H. *Annual review of physical chemistry* **1990**, *41*, 525-557.
- (123) Hamley, I. W.; Hamley, I. W.: *The physics of block copolymers*; Oxford University Press Oxford, 1998; Vol. 19.
- (124) Leibler, L. *Macromolecules* **1980**, *13*, 1602-1617.
- (125) Matsen, M. W.; Bates, F. S. *Macromolecules* **1996**, *29*, 1091-1098.
- (126) Phillip, W. A.; Hillmyer, M. A.; Cussler, E. L. *Macromolecules* **2010**, *43*, 7763-7770.
- (127) Bockstaller, M. R.; Mickiewicz, R. A.; Thomas, E. L. *Advanced Materials* **2005**, *17*, 1331-1349.
- (128) Yao, L.; Lu, X.; Chen, S.; Watkins, J. J. *Macromolecules* **2014**, *47*, 6547-6553.
- (129) Mansky, P.; Liu, Y.; Huang, E.; Russell, T.; Hawker, C. *Science* **1997**, *275*, 1458-1460.

- (130) Albert, J. N.; Epps III, T. H. *Materials Today* **2010**, *13*, 24-33.
- (131) Xiang, H.; Shin, K.; Kim, T.; Moon, S. I.; McCarthy, T. J.; Russell, T. P. *Macromolecules* **2004**, *37*, 5660-5664.
- (132) Kim, S. O.; Solak, H. H.; Stoykovich, M. P.; Ferrier, N. J.; de Pablo, J. J.; Nealey, P. F. *Nature* **2003**, *424*, 411.
- (133) Park, M.; Harrison, C.; Chaikin, P. M.; Register, R. A.; Adamson, D. H. *Science* **1997**, *276*, 1401-1404.
- (134) Arsenault, A. C.; Rider, D. A.; Tétreault, N.; Chen, J. I. L.; Coombs, N.; Ozin, G. A.; Manners, I. *Journal of the American Chemical Society* **2005**, *127*, 9954-9955.
- (135) Kim, M.; Mun, J.; Bae, D.; Jeon, G.; Go, M. C.; Rho, J.; Kim, J. K. *NPG Asia Materials* **2018**, *1*.
- (136) Phillip, W. A.; O'Neill, B.; Rodwogin, M.; Hillmyer, M. A.; Cussler, E. *ACS applied materials & interfaces* **2010**, *2*, 847-853.
- (137) Choi, W. T.; Song, J.; Ko, J.; Jang, Y.; Kim, T. H.; Han, Y. S.; Lim, J.; Lee, C.; Char, K. *Journal of Polymer Science Part B: Polymer Physics* **2016**, *54*, 128-134.
- (138) Ko, J.; Song, J.; Yoon, H.; Kim, T.; Lee, C.; Berger, R.; Char, K. *Advanced Materials Interfaces* **2016**, *3*, 1600264.
- (139) Thurn-Albrecht, T.; Schotter, J.; Kästle, G.; Emley, N.; Shibauchi, T.; Krusin-Elbaum, L.; Guarini, K.; Black, C.; Tuominen, M.; Russell, T. *Science* **2000**, *290*, 2126-2129.
- (140) Klinger, D.; Wang, C. X.; Connal, L. A.; Audus, D. J.; Jang, S. G.; Kraemer, S.; Killops, K. L.; Fredrickson, G. H.; Kramer, E. J.; Hawker, C. J. *Angewandte Chemie* **2014**, *126*, 7138-7142.
- (141) Koneripalli, N.; Singh, N.; Levicky, R.; Bates, F. S.; Gallagher, P. D.; Satija, S. K. *Macromolecules* **1995**, *28*, 2897-2904.
- (142) Li, L.; Matsunaga, K.; Zhu, J.; Higuchi, T.; Yabu, H.; Shimomura, M.; Jinnai, H.; Hayward, R. C.; Russell, T. P. *Macromolecules* **2010**, *43*, 7807-7812.
- (143) Ma, M.; Krikorian, V.; Yu, J. H.; Thomas, E. L.; Rutledge, G. C. *Nano letters* **2006**, *6*, 2969-2972.
- (144) Shin, J. M.; Kim, Y.; Yun, H.; Yi, G.-R.; Kim, B. J. *ACS nano* **2017**, *11*, 2133-2142.

- (145) Wu, Y.; Cheng, G.; Katsov, K.; Sides, S. W.; Wang, J.; Tang, J.; Fredrickson, G. H.; Moskovits, M.; Stucky, G. D. *Nature materials* **2004**, *3*, 816.
- (146) Yabu, H.; Higuchi, T.; Jinnai, H. *Soft Matter* **2014**, *10*, 2919-2931.
- (147) Bosse, A. W.; Garcia-Cervera, C. J.; Fredrickson, G. H. *Macromolecules* **2007**, *40*, 9570-9581.
- (148) He, X.; Song, M.; Liang, H.; Pan, C. *The Journal of Chemical Physics* **2001**, *114*, 10510-10513.
- (149) Matsen, M. *The Journal of chemical physics* **1997**, *106*, 7781-7791.
- (150) Bae, D.; Cho, W. J.; Jeon, G.; Byun, J.; Kim, J. K. *The Journal of Physical Chemistry C* **2012**, *116*, 26523-26528.
- (151) Baek, K. M.; Kim, J. M.; Jeong, J. W.; Lee, S. Y.; Jung, Y. S. *Chemistry of Materials* **2015**, *27*, 5007-5013.
- (152) Choi, H. K.; Chang, J.-B.; Hannon, A. F.; Yang, J. K.; Berggren, K. K.; Alexander-Katz, A.; Ross, C. A. *Nano Futures* **2017**, *1*, 015001.
- (153) Ryu, Y.; Kang, G.; Lee, C.-W.; Kim, K. *RSC Advances* **2015**, *5*, 76085-76091.
- (154) Fleischer, M.; Weber-Bargioni, A.; Altoe, M. V. P.; Schwartzberg, A. M.; Schuck, P. J.; Cabrini, S.; Kern, D. P. *ACS nano* **2011**, *5*, 2570-2579.
- (155) Horrer, A.; Schäfer, C.; Broch, K.; Gollmer, D. A.; Rogalski, J.; Fulmes, J.; Zhang, D.; Meixner, A. J.; Schreiber, F.; Kern, D. P. *small* **2013**, *9*, 3987-3992.
- (156) Hu, Y. S.; Jeon, J.; Seok, T. J.; Lee, S.; Hafner, J. H.; Drezek, R. A.; Choo, H. *Acs Nano* **2010**, *4*, 5721-5730.
- (157) Toma, M.; Loget, G.; Corn, R. M. *Nano letters* **2013**, *13*, 6164-6169.
- (158) Bae, D.; Jeon, G.; Jinnai, H.; Huh, J.; Kim, J. K. *Macromolecules* **2013**, *46*, 5301-5307.
- (159) Lee, D.; Kim, M.-H.; Bae, D.; Jeon, G.; Kim, M.; Kwak, J.; Park, S. J.; Kim, J. U.; Kim, J. K. *Macromolecules* **2014**, *47*, 3997-4003.
- (160) Jinnai, H.; Spontak, R. J.; Nishi, T. *Macromolecules* **2010**, *43*, 1675-1688.

국문초록

서로 다른 동중중합체가 공유결합으로 이어진 블록공중합체(Block Copolymers)는 자기조립과정을 통해 판상형, 원기둥형, 구형과 같이 다양한 형태를 갖는 나노크기 수준의 미세구조를 형성할 수 있다. 이러한 나노구조를 부합하는 목적에 맞게 다양화하고 제어하기 위해 전자기장, 표면처리, 가둠효과 등과 같은 다양한 방법들이 연구되어 왔다. 특히 이 중에서 나노가둠효과(Nano-Confinement)를 이용할 경우 블록공중합체는 기존의 벌크(Bulk)상태에서 나타나지 않던 새롭고 독특한 구조들을 만들어 낼 수 있다. 이러한 가둠효과를 조절하여 다양한 형태의 나노구조를 잘 제어할 수 있다면, 구조적 특성이 중요한 리쓰그래피 공정, 광결정, 플라즈모닉스(Plasmonics), 여과 공정, 광전소자 등의 개발에 활용될 수 있다. 본 연구에서는 이러한 나노가둠효과가 블록공중합체가 자기조립되어 만드는 나노구조에 미치는 영향을 연구하였다. 각 장의 주요 내용은 다음과 같다.

제 1 장에는 나노공간에 가두어진 블록공중합체의 상분리에 대한 연구에 수록되어 있다. 나노가둠효과는 가둠을 주는 방향의 차원에 따라 박막과 같은 1 차원, 기공막과 같은 2 차원 그리고, 에멀전과 같은 3 차원으로 분류될 수 있다. 고분자 사슬 정도의 크기를 갖는 구조체 내에 가두어진 블록공중합체의 자기조립구조는 고분자 사슬 자체의 특성에 더해 이를 가두고 있는 환경의 크기, 구조, 표면성질 등에도 영향을 받는다. 본 연구에서는 이러한 가둠효과 중에서 다공성 음극산화

알루미늄을 이용한 2 차원의 나노크기 공간에 블록공중합체를 가두고 상분리 구조를 조절하기 위해 다양한 형태의 가둠환경을 조성하였다. 이를 통해 블록공중합체의 구조를 제어할 수 있는 다양한 인자들을 조절하며 구조적 변이를 분석하고 그 기저에 있는 블록공중합체의 열역학적 배경을 연구하였다.

제 2 장에서는 블록공중합체를 가둘 수 있는 다양한 형태의 나노기공을 갖는 음극 산화 알루미늄 템플레이트(Anodic Aluminum Oxide Template; AAO) 를 만드는 과정에 대해 정리되어 있다. 특히 비등방적인 구조의 기공을 설계하여 가두어진 고분자 사슬이 만드는 조립구조의 대칭성을 깨뜨리고 기존에 관찰되지 않았던 새로운 나노구조를 만들 수 있는 기반을 연구하였다. XY평면에 대해 비등방적인 삼각기둥 기공은 기존에 잘 알려진 음극산화 알루미늄의 오목한 패턴을 전사하여 설계하고, Z축에 대해 비등방적인 원뿔형 기공은 기공을 자라게 하는 전기적 산화반응과 기공을 확장시키는 식각과정을 번갈아 반복하여 만들 수 있었다. 또한, 이러한 다양한 형태의 나노기공들은 그 구조가 정렬되어 있어서 다른 물질의 나노구조체를 만드는 틀로도 사용될 수도 있다. 이를 위해 나노임프린팅 방법을 통해 고분자 물질로 패턴을 전사하는 연구 역시 함께 수행하였다.

제 3 장에서는 원기둥형 기공 내에 가두어진 블록공중합체의 나노구조를 제어하기 위해 동중중합체를 첨가하거나 기공 내벽의 표면을 개질하는 두 가지 연구에 대해 기술하였다. 우선, 원기둥형 나노기공 내에서 블록공중합체와 함께 동중중합체를 넣어 나노구조가 어떻게

변이하는지 벌크상태와 비교하며 분석하였다. 이를 통해 동중중합체의 분자량과 비율에 따라 자기조립구조의 변화가 다른 양상으로 일어나는 것을 확인하였다. 특히, 곡률의 특성이 더해져 가둠효과가 크게 나타나는 원기둥형 기공 내에서 동중중합체로 인한 상변이가 벌크상태에 비해 더 강하게 나타나고, 동중중합체의 구배 역시 고분자 사슬의 움직임이 가장 제한되는 기공의 제일 안 쪽에 집중되는 것을 확인하였다. 두번째로는 원기둥형 나노기공 내벽에 온도에 따라 표면에너지 조절이 가능한 유기실리케이트(Organosilicate)를 코팅하여 가두어진 블록공중합체의 구조의 배향을 조절하는 연구를 수행하였다. 유기실리케이트의 표면 에너지를 조절함에 따라 동심원구조나 쌓인판 (Staked Disk)와 같은 배향이 전혀 다른 구조들을 구현할 수 있었다. 이러한 연구들은 이차원 공간에 가두어진 블록공중합체의 자기조립 구조를 제어하는 필요한 근본적인 배경을 제공할 수 있을 것이다.

제 4 장은 비등방적인 구조를 갖는 원뿔형 기공 내에 가두어진 블록공중합체의 자기조립구조와 이를 조절하기 위한 방안에 대해 연구한 것이다. 기존에 가둠효과 연구에 많이 사용된 환경은 원기둥이나 구와 같은 등방적인 구조였지만, 이와 다르게 원뿔형 기공은 가둠의 정도가 깊이에 따라 점진적으로 커지고 곡률이 매우 큰 꼭지점을 가지고 있는 특성 때문에 기존에 알려진 블록공중합체의 구조와 다른 특성을 기대할 수 있다. 종횡비와 같은 기공의 크기, 꼭지점의 곡률, 표면에너지 등의 조절을 통한 체계적인 분석으로 원뿔형 기공 내에서 블록공중합체의 자기조립에 미치는 열역학적 요소들을 영향을 확인하고 비교할 수

있었다. 특히 꼭지점에서의 매우 큰 곡률은 고분자 사슬의 엔트로피적 에너지의 큰 감소를 만들어 원뿔형 기공 내에서 블록공중합체의 배향을 결정하는 중요한 요소가 되었다. 실험적으로 관찰한 구조를 시뮬레이션 계산 결과와 비교하여 열역학적인 요소들이 블록공중합체의 자기조립 구조에 미치는 영향을 정량적으로도 확인할 수 있었다. 다양한 요소들을 통해 조절이 용이한 블록공중합체의 삼차원적인 나노구조는 금속 코팅과 같은 추가 공정을 통해 광학소자에 활용될 수 있을 것이다.